ISTITUTO NAZIONALE DI FISICA NUCLEARE - ISTITUTO NAZIONALE DI FISICA NUCLEARE - ISTITUTO NAZIONALE DI FISICA NUCLEARE - ISTITUTO NAZIONALE DI FISICA NUCLEARE - ISTITUTO NAZIONALE DI FISICA NUCLEARE - ISTITUTO NAZIONALE DI FISICA NUCLEARE - ISTITUTO NAZIONALE DI

Laboratori Nazionali di Frascati

Submitted to Phys. Rev. D

LNF-90/052(P)
14 Giugno 1990

C. Forti, H. Bilokon, B.d'Ettorre Piazzoli, T.K. Gaisser, L.Satta, T.Stanev:

SIMULATION OF ATMOSPHERIC CASCADES AND DEEP UNDERGROUND MUONS

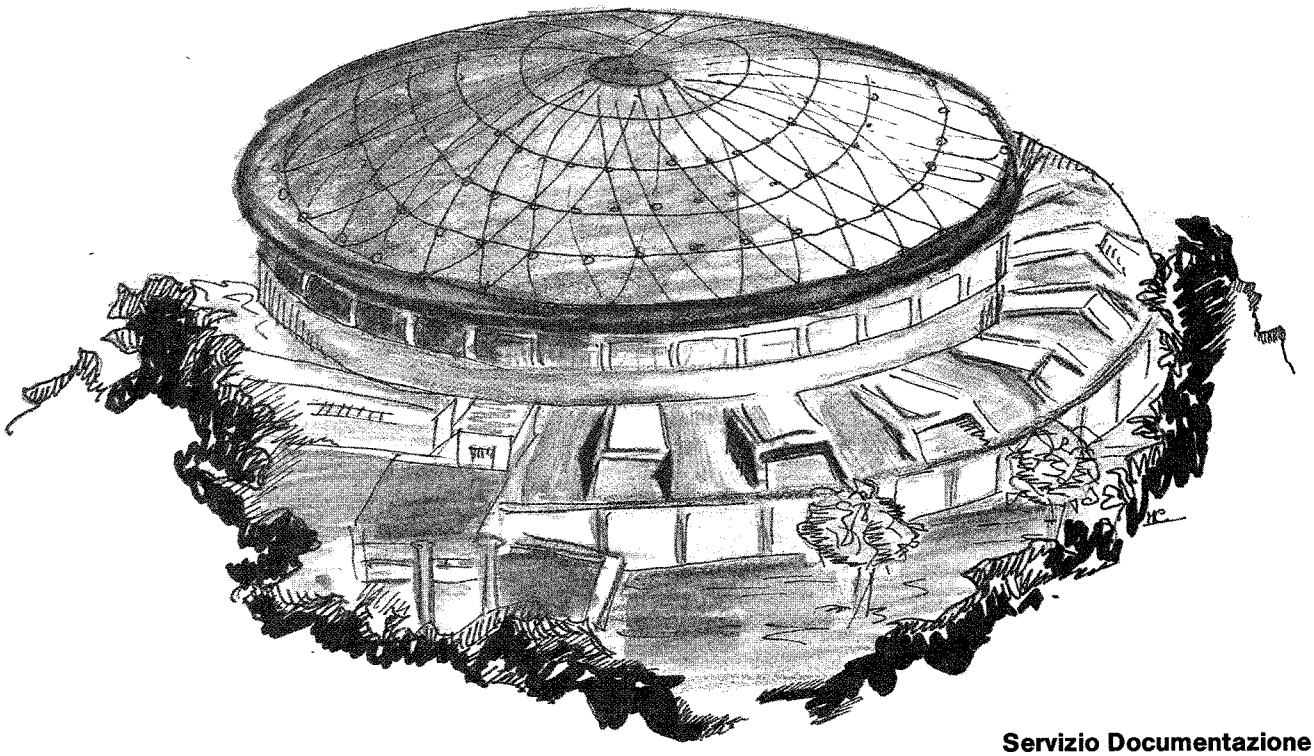

Servizio Documentazione
dei Laboratori Nazionali di Frascati
P.O. Box, 13 - 00044 Frascati (Italy)

INFN - Laboratori Nazionali di Frascati
Servizio Documentazione

LNF-90/052(P)
14 Giugno 1990

SIMULATION OF ATMOSPHERIC CASCADES AND DEEP UNDERGROUND MUONS

C. Forti[1], H. Bilokon[1], B.d'Ettorre Piazzoli[2], T.K. Gaisser[3], L.Satta[1*], T.Stanev[3]

1) Laboratori Nazionali di Frascati - INFN - Frascati (Rome) Italy
2) Istituto di Cosmogeofisica del CNR - Torino, Italy
3) Bartol Research Institute, University of Delaware - Newark (Delaware) USA

ABSTRACT

We describe a new hadronic interaction model for the calculation of high energy cosmic ray cascades in the atmosphere. High energy muons above .5 TeV at production are transported through 7000 hg/cm^2 of rock in order to obtain the multiplicity and lateral distributions at different depths. These distributions are parametrized to facilitate the calculation of the muon bundle rates deep underground. As an illustration, these results are applied to calculate the rates of coincident multiple muons in a detector of finite area at the Gran Sasso Laboratory. We study in particular the sensitivity of rates of high multiplicity events to chemical composition of the primary cosmic radiation and to uncertainties in the interaction model. Our results point to the importance of coincident measurement of showers at the surface to maximize the power of an underground detector to study the primary composition.

I. INTRODUCTION

Elemental composition and energy spectrum of primary cosmic rays are intimately linked to their galactic evolution. Thus, the knowledge of these properties may provide information useful to discriminate between competing theories of the origin of cosmic rays, their acceleration and propagation through the galactic volume. The search for ultrahigh energy

*also Physics Department, University of L'Aquila, 67100 L'Aquila (Italy)

gamma ray (UHE>10^{14} eV) sources is another aspect of the problem of the origin of cosmic rays. In fact, were the detection of UHE gamma rays confirmed, it would imply that these sources accelerate charged hadrons with energies up to about 10^{17} eV. Despite the great astrophysical interest, energies above the TeV region are inaccessible to direct observations due to the flux limitations, and can be investigated only indirectly by studying the properties of secondary particles produced in atmospheric cascades. Thus, progress in these fields depends on the availability of accurate simulations of the cosmic ray induced air showers.

The sensitivity of air shower experiments has been limited producing contradictory interpretations of the properties of the primary cosmic ray beam above 10^{13} eV. New arrays now in a design or construction stage, will attack this problem with improved accuracy in sampling the various components of extensive air showers. As a pertinent example, we mention the recent starting of combined measurements of the electron component at surface and high energy muons deep underground at the Gran Sasso Laboratory[1]. The surface array, EAS-TOP, will also provide the sampling over a large area (~150 m^2) of the muon density (E_μ>2 GeV) and the high energy hadron (E_h~0.5÷10 TeV) content near the shower core.

Recent data from collider experiments provide the characteristic features of the nucleon-nucleon interaction at energies up to 10^{15} eV and allow the development of reasonable models of the atmospheric cascade, even though the kinematical regions covered by accelerator and cosmic ray experiments are only partially overlapping and some uncertainty remains in describing the properties of the particle production in nucleus-nucleus interactions.

This paper is devoted to the presentation of a Monte Carlo code to follow the Hadronic, Electromagnetic and Muonic components in Air Showers (HEMAS) initiated by hadron primaries. Based mainly on a previous simulation developed by J.A. Wrotniak[2] and by Gaisser and Stanev[3], the HEMAS code describes the multiple hadron production by means of a multicluster model reproducing the observed features at collider energies and extended to include the nuclear target effects. Extrapolation to the highest energies (10^{17} eV) beyond the accelerator region is made in the context of the inelastic 'lns physics'. In the present version (HEMAS-1) the interaction and decay processes in the atmosphere are simulated only for hadrons (π, K and N) and muons above 500 GeV. Electromagnetic particles (γ and $e^{\pm}$) are not followed by the Monte Carlo; however, the total size of each shower (N_e) is calculated at ground level by using an analytic formula for the contribution of each γ, $e^{\pm}$ and subthreshold hadron. A three-dimensional Monte Carlo simulation of the muon propagation through the rock has been coupled to the cascade program in order to generate muon events deep underground. In this configuration HEMAS is an adequate tool to interpret the muon bundle events observed in underground detectors and has already been applied in the analysis of data from the NUSEX experiment[4] to study the composition of the primary cosmic ray radiation in the energy region from 10^{12} to 10^{17} eV.

The paper is organized as follows. In section II we describe in detail the interaction model. Then we briefly summarize the main features of the simulation of the muon propagation through the rock in section III. Section IV contains parametrizations of the muon multiplicity

and lateral displacement distributions deep underground, based on the Monte Carlo results. As suggested in Ref.3 parametrizations of the results of the Monte Carlo can be used as a substitute for generation of complete events. This procedure is relatively very fast (~ 30 ms per event compared to ~5 s per shower at 1000 TeV). These parametrizations do not depend on any particular experimental configuration; once inserted in an event generator provided with the map of a specific mountain, with the rock characteristics (density and chemical composition) and with the apparatus geometry, they are particularly useful for determining the power of an experiment to discriminate between different compositions and for the analysis of the multiple muon data. In section V we discuss the dependence of the underground muon results on the hadron-air interaction model. In section VI we illustrate the use of the parametrizations by calculating event rates in detectors of different sizes at Gran Sasso.

II. INTERACTION MODEL

The mean proton path length in the atmosphere $\lambda_{p\text{-}air}$ is related to the proton-air inelastic cross section $\sigma_{p\text{-}air}$ by :

$$\lambda_{p\text{-}air}(g/cm^2) = \frac{2.4 \cdot 10^4}{\sigma_{p\text{-}air}(mbarn)} \qquad (1)$$

with similar relations for the other hadrons. Cross sections of hadrons on nuclei are not measured directly at energies greater than several hundred GeV. The relation to proton-proton cross sections is rather well understood and can be used[5] to extend the hadron-nucleus cross sections to energies equivalent to $E_{lab} \geq 100$ TeV. Extrapolations to higher energies are more model-dependent. In these calculations we have used a set of formulas traditionally used in cosmic ray calculations[6], which have the form $\sigma \sim a+b\cdot[\ln(s)]^{1.8}$ These are represented by continuous curves in figure 1. For comparison, and to explore the sensitivity of the calculation of the muon parameters to the assumed cross sections, we have also made some test runs using the cross sections shown as dashed lines in figure 1. The dashed lines are obtained from an extrapolation of the pp cross section due to Durand and Pi[7]. The corresponding p-nucleus cross sections are obtained using the relation of Ref.5. The dashed lines for mesons are calculated similarly to the calculation of Ref.7 for protons [S. Tilav, private communication]. The results of this test are reported in section V.

In the hadron-air interaction model[8] the particles are produced in clusters according to the more recent theoretical[9] and experimental[10] considerations. The algorithm for pp and $p\bar{p}$ interactions is close to the GENCL code developed at CERN by the UA5 collaboration[10]. It was first written and checked against pp data at $\sqrt{s}$=53 GeV and against $p\bar{p}$ data from $\sqrt{s}$=53 to 900 GeV. Then, the effects of the nuclear target mass were included in the model. The interaction model is described in detail in the remainder of this section.

A. Non single diffractive pp and $p\bar{p}$ events

The steps of the Monte Carlo algorithm are, for non single diffractive (NSD) events:

a) choose the number of charged hadrons n_{ch} from a negative binomial (NB) distribution[11] :

$$P(n_{ch}) = \begin{bmatrix} n_{ch}+k-1 \\ n_{ch} \end{bmatrix} \cdot \left(\frac{<n_{ch}>/k}{1+<n_{ch}>/k}\right)^{n_{ch}} \cdot \left(\frac{1}{1+<n_{ch}>/k}\right)^{k} \quad (2)$$

with $\begin{bmatrix} n+k-1 \\ n \end{bmatrix} = k\,(k+1)\,\ldots\,(k+n-1)\,/\,n!$

with an energy dependence of the parameters given by :

$$<n_{ch}> = -7.0 + 7.2\ s^{0.127} \quad (3)$$

$$k^{-1} = -0.104 + 0.058 \cdot \ln(\sqrt{s}) \quad (4)$$

with s in GeV^2.

b) choose the nature of the leading particles (p or n or their antiparticles) :
   - in $p\bar{p}$ interactions the probability of charge exchange p—>n (or $\bar{p}$—>$\bar{n}$) is taken from Ref.10 ;
   - for pp interactions the charge exchange probability (~40%) was deduced from the mean proton and the mean neutron multiplicity measured at ISR[12,13], and was considered energy independent. The resulting mean inelasticities at E_{lab}=150 TeV ($\sqrt{s}$~540 GeV) are, respectively, 0.52 for the non charge-exchange process and 0.63 for the charge-exchange one.

c) produce a given number of kaons.
   The kaons are grouped into pairs (clusters) of zero strangeness including pairs with neutral kaons and with kaon resonances. The pairs K^+K^-, $K^+\bar{K}^o$, K^0K^-, and $K^0\bar{K}^o$ have all the same production probability and each kaon is a K^* with 60% probability, according to ISR measurements[14]. The actual number of kaon clusters is drawn from a Poisson with mean deduced from the K/π ratio[8, 15]

$$<K^{\pm}>/<\pi^{\pm}> = 0.056 + 0.00325 \cdot \ln s \quad (5)$$

   Then, the K^*'s decay into $K\pi$ pairs.

d) regroup the remaining charged particles (pions) into clusters that include an admixture of neutral pions to give the observed correlation[10] between the photon multiplicity n_γ and n_{ch} :

$$< n_\gamma > = 2 + 1.030 \cdot n_{ch} \quad (6)$$

e) choose the masses of the pion clusters from a gaussian distribution with a mean that depends on the number of pions in a manner[16] related to the masses of pion resonances, such as the ρ ;

f) give an excitation energy E to each kaon cluster, chosen from an exponential distribution :

$$dN/dE^2 = \text{constant}\cdot\exp(-2\cdot E/b) \tag{7}$$

where the value 0.75 GeV for the b parameter provides the correct $\langle p_t \rangle$ for the charged kaons[10] ;

g) choose the transverse momentum of the leading nucleons and of the meson clusters from an exponential-law distribution :

$$\frac{dn}{dp_t^2} = \text{constant}\cdot e^{-b\,p_t} \tag{8}$$

where b=6 $(GeV/c)^{-1}$, or from an inverse power-law distribution :

$$\frac{dn}{dp_t^2} = \frac{\text{constant}}{(p_t^o + p_t)^{\alpha}} \tag{9}$$

where p_t^0=3 GeV/c while α decreases logarithmically with energy :

$$\alpha = 3 + \frac{1}{0.01 + 0.011\cdot\ln s} \tag{10}$$

For the single pion clusters the p_t is always sampled from the distribution (8). For the pion clusters with at least two particles, for the kaon clusters and for the leading nucleons, the probability for using (9) increases in proportion to the number of clusters in the event. This reproduces the increase of the transverse momentum with the event multiplicity, reported by the UA1 experiment[17]. Moreover, as a consequence of the energy dependence of α, the $\langle p_t \rangle$ of all charged particles increases logarithmically with energy, according to the UA5 results[15]. In Fig.2 we show the Monte Carlo results for the p_t distribution at $\sqrt{s}$=540 GeV compared with a parametrization of the UA1 data[18];

h) the azimuthal angles of the leading nucleons and of the meson clusters are chosen randomly between 0 and 2π. Then, the resulting momenta, p_x and p_y, of each cluster, in the plane perpendicular to the beam direction (z), are translated in such a way that there is conservation of the x and y components of the total momentum ;

i) the C.M. rapidities of the leading nucleons and of the N_{cl} meson clusters are chosen in three steps :

1. sample N_{cl}+2 values of the so-called pre-rapidity, from a distribution with a central plateau and two gaussian wings[10];
2. choose between these N_{cl}+2 values the ones corresponding to the leading nucleons. The leading forward (backward) is given the highest (smallest) pre-rapidity with a high probability. This probability is adjusted to get the desired shape of the leading particle

Feynman x (x_F) distribution[19,13] in pp interactions at $\sqrt{s}$=53 GeV. The pre-rapidities of the meson clusters are chosen randomly among the N_{cl} remaining values.

3. the pre-rapidities y' are then transformed into the true rapidities y using y = A + By', where A is determined from the total longitudinal momentum conservation, and B from the total energy conservation[20];

j) finally, the clusters decay isotropically in the cluster rest frame and each particle is transformed first to the nucleon-nucleon C.M. system, then to the lab frame.

The technique of rapidity sampling just described reproduces the rapidity distribution at various energies (Fig.3) - with the increase of the particle density in the central rapidity region - and the correlation between rapidity and multiplicity of charged hadrons (Figs.4 and 5).

B. Target effects in non-diffractive events

We have modified the nucleon-nucleon event generator in order to include the nuclear target effects, while retaining the correlations among transverse momentum, multiplicity and energy.

a) the number of charged hadrons is still sampled from a negative binomial distribution.The average $\langle n_{ch} \rangle$ in p-air collisions is obtained by integrating the expected inclusive rapidity distribution dn_{ch}/dy which is calculated at any energy by using the relation between the rapidity density with a nuclear target and that with a target nucleon. This relation has been investigated by Voyvodic[25] analyzing data on rapidity and pseudorapidity distributions for various nuclear targets at lab energies from 24 GeV to 400 GeV. He showed that the ratio R_A of the rapidity density with a nuclear target of mass A to the rapidity density with a target nucleon can be satisfactorily parametrized by means of a single function $\beta(z)$ of the scaling variable z=y/lns :

$$\frac{dn/dy\ (p\text{-}A)}{dn/dy\ (p\text{-}p)} = R_A(z) = A^{\beta(z)} \tag{11}$$

where y is the lab rapidity. The function $\beta(z)$ calculated from the considered set of data, depends neither on the target mass A, nor on the C.M. energy $\sqrt{s}$ over the range studied. The relation (11) has been used to derive the rapidity distribution in p-air collisions from the rapidity distribution in pp collisions. We took $\langle A \rangle$=14.5 and calculated the function $R_A(z)$ for air nuclei[8].

To obtain the pp rapidity distribution, we have used the measured rapidity distribution in $p\bar{p}$ NSD interactions. In the range $\sqrt{s}$=53÷900 GeV, this distribution can be described[26] by a single function $F(\xi)$ of the scaling variable $\xi=y^*/y_o^*$, where y^* is the C.M. rapidity and $y_o^*=\ln\sqrt{s}$:

$$F(\xi) = \frac{1}{(y_o^*)^2 \cdot \sigma_{inel}} \cdot \frac{d\sigma}{d\xi} = a\cdot\left(1+ b\left|\xi\right|\right)\cdot e^{-c\left|\xi\right|^d} \tag{12}$$

with a=0.485, b=0.6, c=2.7 and d=3.0.

We assume the validity of the relations (11) and (12) holds beyond the energy region of the measurements. In Fig.6 the expected rapidity distribution for p-air collisions at $\sqrt{s}$=10 TeV (curve 2) is compared to that calculated for p-p collisions (curve 1). The area under the curve 1 (~63.3) represents the average multiplicity of charged particles in pp non-diffractive collisions, quite close to the result (67.7) provided by the formula (3), actually used in the simulation of the p-p interactions.The increase of the multiplicity of charged particles produced in p-air interactions, relative to the multiplicity in p-p interactions derives from the intranuclear cascading of particles that are slow enough to materialize inside the nucleus. As a consequence, in p-air collisions the backward particle production ($<n_{ch}>$backw.~61.0, in Fig.6) exceeds the forward particle production ($<n_{ch}>$forw.~38.8) and the distribution gets asymmetric in the C.M. projectile-target nucleon. The negative binomial k parameter of the forward hemisphere of p-nucleus collisions is known to be independent of the target mass and identical to that in pp collisions[27]. In the backward hemisphere the k parameter does depend on the target mass[27], but the energy dependence of this effect is not known. For simplicity, therefore, we neglect the backward excess and use a distribution that is symmetric about y^*=0 in the projectile-target nucleon C.M. (see the dashed curve in Fig.6). The average charged multiplicity in a p-air collision is thus taken as twice the charged particle rapidity density integrated over the forward C.M. hemisphere and the k parameter also is taken as symmetric (Eq.4). This simplification makes a negligible error in the calculation of deep underground muons because it does not affect the forward particles. For example, even at an energy as high as $\sqrt{s}$=10 TeV (equivalent to $E_{lab}=5.3\cdot10^{16}$ eV), the backward charged hadrons that we neglect to produce, which represent on average about 20% of the total charged multiplicity, would carry less than 10^{-4} of the total energy E_{lab}. Of these hadrons, less than 3% would have more than 1 TeV (that represents approximately the threshold energy for a muon to transverse 3000 hg/cm^2 of standard rock).

b) the nature of the leading nucleons is determined from the cross section for the charge-exchange process p+Be—>n+anything, compared to the cross section for the non charge-exchange process p+C—>p+anything[28].

Steps c, d, e and f are carried out as for pp collisions.

g) the transverse momentum distribution in p-nucleus collisions has been measured at 300 GeV/c on various targets[29]. The ratio $R_{A,i}(p_t)$ of the inclusive cross section on a target of mass A to that on a proton target for production of a particle of type i (i=π,K,p) has been parametrized in the form:

$$R_{A,i}(p_t) = A^{\alpha_i(p_t)} \tag{13}$$

where the α_i are functions of p_t, slightly different for each particle type. We approximated the functions R_i with a single function R, for all particle types :

$$\begin{aligned} R(p_t) &= (0.0363\cdot p_t + 0.0570)\cdot K \quad && \text{for } p_t \le 4.52 \text{ GeV/c} \\ R(p_t) &= 0.2211\cdot K && \text{for } p_t > 4.52 \text{ GeV/c} \end{aligned} \tag{14}$$

where the normalization constant K is irrelevant for the p_t sampling. The transverse momentum of the leading nucleons and of the meson clusters is chosen from the exponential or the power-law distribution as in section 1g, but with each distribution (8) and (9) multiplied by $R(p_t)$ and renormalized to 1. We verified the consistency of applying the correction factor (13) to the cluster distributions even though it was determined experimentally for particle distributions. We assume that the shape of R is energy independent.

h) the azimuthal angles of the final particles are chosen as for pp collisions;

i) the pre-rapidity of the clusters is assigned as in pp collisions; however, the algorithm for assigning the forward leading nucleon pre-rapidity is modified to make the resulting leading nucleon elasticity distribution softer in p-nucleus collisions. Sampling of the leading nucleon pre-rapidity has been tuned in order to reproduce the results quoted by Jones[28] concerning the x_F distribution in p-Carbon collisions at 100 GeV and in p-Beryllium collisions at 300 GeV as shown in Fig. 7. Direct comparison of these distributions with those from the p-air model is possible because the carbon and beryllium masses are close to the average air mass and because the leading x_F distribution exhibits a slow dependence on the target mass.

j) cluster decay and transformation to the lab frame are the same as for pp.

Our model for p-air interaction assumes a scaling violation in the central rapidity region, according to the results obtained at ISR and at CERN collider energies[30]. As a consequence, in going from a beam energy E_{lab}=1 TeV to 10^4 TeV, the mean number of charged pions with x_F<0.05 grows by a factor of about F=7. Concerning the extreme fragmentation region (x_F>0.50), where there are no data available from the $p\bar{p}$ collider experiments, our model predicts a small (F=1.60) scaling violation effect (Fig.8).

We studied the x_F distribution of the hadronic parents of the underground muons. We found that for primary vertical protons of energy between 10^{14} and 10^{16} eV and for rock thicknesses between 3000 and 6000 hg/cm^2, the fraction of muons whose parents have x_F>0.50 is about 10-15%, while about 45-60% of the muons are produced by the decay of hadrons with x_F<0.10.

C. Non-diffractive interactions of π and K on air

While the model of pp and $p\bar{p}$ collisions is based on data that extends up to $\sqrt{s}$=900 GeV, which is equivalent to $E_{lab} \approx 430$ TeV, meson cross sections have only been measured up to a few hundred GeV lab energy. Thus, we have simulated the interactions of pions and kaons using an appropriately modified version of the p-air model. In particular, the main difference between the meson and the proton interactions is that the former have a weaker leading effect than the latter. Accordingly, the forward leading meson pre-rapidity is chosen in such a way that the probability for the leading meson to have the largest pre-rapidity is smaller than for a

leading nucleon. The Monte Carlo has been tuned (Fig.9) to the experimental data[31] of the x_F distribution of charged pions obtained in interactions of π^+ and K^+ on a Carbon target.

D. Single diffractive hadron-air events

Single diffractive events (projectile fragmentation only) are generated in a fraction F_d of all inelastic collisions, very slightly decreasing with energy :

$$F_d = 0.125 - 0.0032 \cdot \ln s \tag{15}$$

F_d is about 10% at ISR energies[32] and 8.5% at CERN Collider energies[33].

In the single diffractive interactions we are considering, the target nucleon is still intact after the collision, while the incident hadron (π, K or nucleon) is excited to a system (diffractive cluster) of higher mass but with the same quantum numbers (charge and strangeness in our simulation), which subsequently decays.

These are the main steps in event generation :

a) sample the mass M of the diffractive cluster using a probability distribution :

$$\frac{dN}{d(M^2/s)} = \frac{\text{constant}}{M^2/s} \tag{16}$$

in agreement with the scaling in M^2/s observed from ISR[34] to CERN Collider[35] energies;

b) sample the 4-momentum transfer squared t (<0) using a distribution :

$$\frac{dN}{d|t|} = \text{constant} \cdot e^{-|t - t_{min}| \cdot b} \tag{17}$$

where the b parameter[36] is 7 $(GeV/c)^{-2}$ and t_{min} is the minimum 4-momentum transfer squared required to produce the mass M ;

c) sample the azimuthal angle ϕ of the target nucleon in the final state, randomly between 0 and 2π ;

d) sample the number n_{ch} of charged particles in the diffractive cluster from a negative binomial distribution, as in the non-diffractive case, but with s replaced by M^2 in the calculation of the $\langle n_{ch} \rangle$ and k parameters, according to recent experimental data[37] ;

e) sample the number of π^0 in the cluster from a Poisson with the mean obtained from the formula (6) taking into account that in our model the π^0's are the only source of gammas ;

f) perform the decay of the cluster into "leading hadron + pions", according to thelongitudinal phase space, in three steps :

1. sample the p_t of each particle from an exponential distribution with $\langle p_t \rangle = 0.45$ GeV/c, assumed independent from the mass M of the cluster ;
2. sample randomly the pre-rapidities of the decay products ;
3. operate, on each pre-rapidity y', a linear transformation y'—>y=A+B·y' (similar to that used for the meson clusters in non-diffractive interactions, see II.A.i) .

g) finally, perform the Lorentz transformations from the cluster rest frame to the C.M. of

the target nucleon and projectile hadron and then to the lab frame.

The same scheme is used for p-p, p-air, n-air, π-air and K-air diffractive interactions.

In Fig.10 the particle density $dn/d\eta$ at the diffractive cluster's kinematical central value $<\eta>=\ln(\sqrt{s}/M)$ is shown as a function of the cluster mass M. The Monte Carlo results are compared with the $p\bar{p}$ SD data of the UA4 collaboration[37] at $\sqrt{s}$=540 GeV. The result obtained assuming isotropic decay for the diffractive cluster, which is consistent with experimental results at ISR energy[38], is shown for comparison. At high energy it is clear that the diffractive cluster does not decay isotropically. Fig.11 shows the pseudorapidity distributions for the mass windows with <M>=20 and <M>=80 GeV. Within the accuracy of the experimental data the shape of these distributions is rather satisfactorily reproduced.

The present version of the Monte Carlo allows us to describe the evolution of high energy hadrons and muons in atmospheric cascades. Minimum threshold is 500 GeV, due to the fact that the algorithm for the transformation of pre-rapidities does not work correctly for lower energies. The collision generator is coupled to other subprograms which allow i) calculation of the electron size by means of a semianalytic approach[39], ii) interaction of incident nuclei with air using either a simple superposition model (independent collisions of nucleons) or an algorithm with a detailed treatment of the nuclear break-up, iii) propagation of the atmospheric muons to the underground detector.

Since the present work is focused on the physics of multiple underground muons, in the following we describe the procedures to calculate the muon yield at the depth of detection. This includes the muon propagation segment and the parametrization of the muon production. For heavy nuclei both the superposition and fragmentation models have been considered and the results compared.

III. MUON PROPAGATION THROUGH THE ROCK

Each muon produced in the atmospheric cascade is transported underground using a three-dimensional Monte Carlo routine[40]. The total rock thickness h is divided into steps Δt. For high energy muons an appropriate choice has been found to be Δt=25 hg/cm^2. Typical energy losses in each step are of the order of a few GeV, which are negligible compared to the initial energy of the muon. Thus the average angular deflection per step changes very slowly from step-to-step. Whenever the muon, in the course of its history, reaches an energy such that the average angular deflection is larger than a limiting value, then the spacing is reduced accordingly. A limiting value of 1 degree has been chosen to keep the desired accuracy without increasing substantially the computing time. For each step, the energy loss is calculated in order to get the average muon energy $<E_\mu>$ along its track. In this calculation[40], ionization[41] and pair production[42] have been treated as continuous processes while bremsstrahlung[43] and nuclear interaction[44] have been treated stochastically. The mean energy $<E_\mu>$ is used for the sampling

of the angular deflection and of the lateral displacement occured in Δt. The use of the gaussian approximation together with an appropriate choice of the mean scattering angle[45] provides results in excellent agreement[40] with those obtained using a complete distribution based on Scott-Snyder-Moliere theory. The correlation between angular and radial displacements is taken into account according to the distributions of Ref.46.

The main uncertainty in the simulation of the muon nuclear interaction, coming from the extrapolation of the photon-nucleon cross section as a function of the photon energy, has been investigated[40]. We find that, if instead of a logarithmically growing cross section (as assumed in the Monte Carlo), we use a constant one, the muon intensity underground for $h \leq 7500$ hg/cm^2 does not change more than 1%. Predictions of this routine concerning the local muon spectrum and angular spread between muon pairs at the Mont Blanc underground laboratory, where the NUSEX detector is operating (at a vertical depth of 5000 hg/cm^2 of standard rock), have been found in excellent agreement with the measured distributions (Refs. 47 and 48 respectively).

IV.PARAMETRIZATIONS FOR UNDERGROUND MUONS

The results of our simulation of atmospheric cascades can be summarized in a set of parametrizations which give the distributions of the muon multiplicity N_μ and of the perpendicular distance of muons from the shower axis R_μ as functions of primary mass, energy and zenith angle and of detector depth. The results obtained here differ from those of Ref.3 mainly in the multiplicity distribution and in the shape of the lateral distribution. However, the mean number of high energy muons is quite similar in the two calculations, and the distributions themselves are not drastically different.

We emphasize that the parametrizations we present here are for muons at the depth of the detector after propagation through the rock. We have made a set of Monte Carlo runs for primary nuclei of mass 1÷56 with energies from 2 to 10^5 TeV/nucleon and zenith angle $0<\theta<60$ degrees. For each event, all muons above 0.5 TeV at production are saved for propagation underground. Table I gives results for the mean number of muons above 0.5 TeV at production, which can be compared with other calculations in a manner that is independent of the treatment of propagation through the rock. Each muon with energy greater than 0.5 TeV is propagated through the rock as described in the previous section and checked for survival to slant depths 3000, 4000, 5000, 6000 and 7000 hg/cm^2 of standard rock (Z=11, A=22). In all cases the altitude of the underground laboratory is taken to be 965 m above sea level, as at Gran Sasso. However, the results depend only weakly (<5%) on this choice because the production height of the muons is much greater (12÷18 km for vertical showers).

The mean number of muons $<N_\mu>$ which go through a rock thickness h, produced by primary cosmic rays of mass A, energy E and zenith angle θ, follows with a good approximation the scaling law :

$$\frac{E_\mu \cdot <N_\mu>}{A \cdot \sec\theta} = f(E_p/E_\mu) \cdot g(E_p/E_\mu) \tag{19}$$

$$g(E_p/E_\mu) = 0.02126 \cdot (E_p/E_\mu)^{0.7068} \cdot (1-E_\mu/E_p)^{9.134} \tag{20}$$

$$f(E_p/E_\mu) = \exp\left[\frac{48.27}{9.467 + (\frac{E_p}{E_\mu})^{3.330}}\right] \tag{21}$$

valid for $E_p/E_\mu > 2$, with the parameter :

$$E_\mu = 0.53 \cdot (e^{4 \cdot 10^{-4} \cdot h} - 1) \tag{22}$$

where h is in hg/cm^2 of standard rock; E_p is the energy per nucleon in TeV.

The function $g(E_p/E_\mu)$ is of the form originally suggested by Elbert[49] to describe the mean number of high energy muons in an atmospheric cascade. Our result for the mean number of muons at the depth of the detector includes a correction factor $f(E_p/E_\mu)>1$ which rapidly approaches one for large values of its argument. We believe that this is a consequence of fluctuations in the survival probability which we have included in the simulation. There is, however, a single relation (Eq.22) between the parameter E_μ and depth. The parametrizations given in Eqs. 19-21 are valid for $E_p/E_\mu>2$. We have checked that the region $E_p/E_\mu<2$ contributes to the single muon rate at the 1% level and is completely negligible for multiple muons.

The muon distributions deep underground are well described by parametrizations which have the same form as the multiplicity distribution and p_t distribution in individual interactions.

The distribution of the multiplicity N_μ is well fitted by a negative binomial function:

$$P(N_\mu) = \begin{bmatrix} N_\mu+k-1 \\ N_\mu \end{bmatrix} \cdot \left(\frac{<N_\mu>/k}{1+<N_\mu>/k}\right)^{N_\mu} \cdot \left(\frac{1}{1+<N_\mu>/k}\right)^{k} \tag{23}$$

with :

$$k = A^{2/3} \cdot 10^{F(<N_\mu>/A)} \tag{24}$$

and :

$$F(<N_\mu>/A) = 0.748 + 0.330 \cdot \log_{10}(<N_\mu>/A) + 0.045 \cdot [\log_{10}(<N_\mu>/A)]^2 \tag{25}$$

The lateral distribution of the muons perpendicular to the shower axis is well reproduced by an inverse power-law form :

$$\frac{1}{N_\mu}\cdot\frac{dN_\mu}{dR_\mu}=\frac{(\alpha\text{-}1)\cdot(\alpha\text{-}2)}{R_o^{2-\alpha}}\cdot\frac{R_\mu}{(R_o+R_\mu)^\alpha} \tag{26}$$

The constant R_o is related to the $\langle R_\mu\rangle$ and α parameters through the formula :

$$R_o=\frac{\alpha-3}{2}\cdot\langle R_\mu\rangle \tag{27}$$

The $\langle R_\mu\rangle$ parameter is given by :

$$\langle R_\mu\rangle = G(E_p, E_\mu, \theta)\cdot\left[11.62\cdot E_\mu^{-0.680}\cdot\left(\frac{E_\mu}{E_p}\right)^{0.114}\cdot\sec\theta\right] \tag{28}$$

where :

$$G(E_p, E_\mu, \theta) = A(E_p, \theta) + B(E_p, \theta)\cdot(E_\mu - 1) \tag{29}$$

$$A(E_p, \theta) = 1.39 - 0.383\cdot X + 6.72\cdot10^{-2}\cdot X^2 + 0.1\cdot(\sec\theta - 1) \tag{30}$$

$$B(E_p, \theta) = [3.14\cdot10^{-2} + 6.65\cdot10^{-3}\cdot(X-1)]\cdot(2 - \sec\theta) \tag{31}$$

with $X=\log_{10}(E_p/1\ \text{TeV})$. The α parameter is :

$$\alpha = C(E_p)\cdot\left[\frac{1.138}{-1.126+\langle R_\mu\rangle} + 0.848\right] \tag{32}$$

with :

$$C(E_p) = \exp\,[\,2.413 - 0.260\cdot X + 0.0266\cdot X^2\,] \tag{33}$$

where $\langle R_\mu\rangle$ is in meters. When $\langle R_\mu\rangle < 1.13$ m the exponential form :

$$\frac{1}{N_\mu}\cdot\frac{dN_\mu}{dR_\mu}=\frac{4}{\langle R_\mu\rangle^2}\cdot e^{-2\,R_\mu\,/\,\langle R_\mu\rangle} \tag{34}$$

must be used instead of the power-law (26).

Figure 12 shows comparisons between the muon multiplicity distribution obtained with the Monte Carlo (histograms), the best fit with a negative binomial (continuous curves) and a Poisson with the same $\langle N_\mu\rangle$ as from the Monte Carlo (dashed curves), for two different values of primary energy. The Poisson is the functional form suggested in Ref.3; for a fixed $\langle N_\mu\rangle$, it represents the limit of the NB when the k parameter tends to infinity. As a consequence, the fluctuation of the multiplicity provided by the NB :

$$\sigma^2 = \langle N_\mu\rangle^2/k + \langle N_\mu\rangle \tag{35}$$

is larger than the fluctuation expected from a Poisson with the same average.

Figure 13 shows comparisons between the lateral displacement distribution obtained with the Monte Carlo (histograms), the best fit with an inverse power-law function (continuous curves) and an exponential distribution with the same $<R_\mu>$ as from the Monte Carlo (dashed curves), as suggested in Ref.3. Here the comparisons are shown for the same primary energies but at different slant depths h and therefore different values of the parameter E_μ. We notice that when the ratio E_μ/E_p decreases (for lower rock thicknesses and/or for greater primary energies), the multiplicity and the lateral distributions exhibit a noticeable deviation from the conventional ones (Poisson and exponential respectively). Note that the lateral distribution is non-exponential at small distances as well as in the tail of the distribution.

The parametrization described here does not incorporate a correlation between muon multiplicity and lateral distribution. We know that such a correlation must exist at some level because events that start unusually high in the atmosphere will tend to produce more muons because the parent mesons decay more easily in the more tenuous part of the atmosphere. To investigate the possible significance of this effect quantitatively, we looked at showers generated by protons at 1000 TeV and zenith angle 28°, as observed at slant depth of 3000 hg/cm^2. In Fig.14 a) we report the mean distance <H> of the muon production point from the sea level as a function of muon multiplicity; Fig.14 b) shows the corresponding mean perpendicular distance of muons from the shower axis. All muons at the depth of the detector are counted. The effect shown here is potentially significant in view of the fact that it is the relative frequency of high multiplicity events that is sensitive to composition at high energy (>10^{14} eV). The fact that events of high multiplicity are more spread out will decrease probability of a proton to generate an event with large N_μ in a finite detector. We expect this correlation to be much less significant for heavy primaries because of the intrinsically smaller fluctuations in showers initiated by heavy nuclei. For example, in a test run with incident iron nuclei of 1000 TeV total energy at 3000 hg/cm^2 and zenith angle 28°, we found no systematic correlation between muon multiplicity and lateral spread of the muons at the detector level. We are investigating the possibility of making a parametrization that includes the correlation between lateral distribution and multiplicity as a function of primary mass, energy, zenith angle and of depth.

To maintain the generality of the parametrizations, we have also neglected the effect of the Earth's magnetic field, which depends on geographic location of the detector and on azimuthal angle of each shower. The relatively small charge separation caused by traversing the geomagnetic field is discussed briefly in Ref.3.

V. DISCUSSION

We have made several assumptions and simplifications in the calculations that lead to the parametrizations described above. In this section we describe these assumptions and assess the associated uncertainties in the results.

A. Cross sections.

To test the sensitivity of the results to the assumed cross sections, we generated 5000 proton showers at 1000 TeV incident energy with 28° of zenith angle, using the two different sets

('a' and 'b') of cross sections already described in section II (in Fig.1 the cross sections of set 'a' are reported as continuous curves; the dashed curves refer to set 'b'). At 1000 TeV the proton air cross sections are :

$$\text{'a'}: \ \sigma_{p\text{-air}} = 416 \text{ mbarn}, \tag{36}$$

$$\text{'b'}: \ \sigma_{p\text{-air}} = 382 \text{ mbarn}, \tag{37}$$

and differ by about 9%. The mean number of muons per shower produced in the atmosphere with energy greater than 1 TeV is decreased by about 5% when the smaller cross section is used. The values of energy used in this test are in the most important energy regions for calculation of multiple muons deep underground.

B. Lambda production.

Lambda production is not included in the calculation. To evaluate the effect of this simplification we ran 5000 proton showers with E_p=1000 TeV at 28°, with and without production of Λ. When Λ production is included with an accompanying kaon (most importantly in the forward fragmentation region) the mean number of muons per shower produced in the atmosphere with energy greater than 1 TeV increases by about 2%.

C. Prompt muons.

Production of prompt muons is not included in the cascade program. Following the arguments of Ref.3, we expect the contribution to muon groups to be unimportant up to slant depths of at least 7 km.w.e., even for an amount of charm production[50] that is larger than now believed possible. For a more recent review of prompt muon production in cosmic rays see Castagnoli et al.[51] .

D. Nuclear target effects.

The introduction of nuclear target effects into the model is the source of some uncertainty because their behavior at high energy (>400 GeV lab energy) depends on an extrapolation of experimental results. We have checked the sensitivity to these assumptions by generating vertical proton showers at E_p=10, 100 and 10^4 TeV with all target effects turned off in the interaction model. This results in decreased inelasticity, decreased $\langle n_{ch} \rangle$ and decreased $\langle p_t \rangle$ relative to hadron-nucleus interactions. Even such an extreme mutilation of the model leads only to modest changes in the properties of the muons. For slant depths between 3000 and 5000 hg/cm^2, $\langle N_\mu \rangle$ increases by 4÷5% for E_p=10 TeV and decreases by about 5% for $E_p \geq 100$ TeV. The mean separation of muons is some 10÷15% smaller for all values of E_p. These changes occur when nuclear target effects are neglected altogether. We therefore conclude that the model of nuclear target effects introduces no significant uncertainty into the properties of the calculated muons.

E. Inelasticity .

An important consequence of this model of hadron-air interactions, in which the final state multiplicity is chosen first for each interaction, is that the mean inelasticity decreases slowly as energy increases, from 0.62 at 1 TeV ($\sqrt{s}$=43 GeV) down to 0.57 at 10^4 TeV ($\sqrt{s}$=4330 GeV). A similar effect has been found in other simulations using multicluster generation[52]. However, there are opposite theoretical predictions about the energy dependence of the

inelasticity above accelerator energies, for example in multiple scattering models of hadronic interactions[53]. In the latter models, energies of the secondary particles are selected first in each event, with the multiplicity of each event determined by the point at which energy is exhausted.

To explore the magnitude of the uncertainty in rates of underground muons from this source, we have generated some events with a low inelasticity model (II) and a high inelasticity model (III). In these models the inelasticity still decreases with the interaction energy, but its values are remarkably different from those obtained with the standard model (I) (see table II). Vertical proton events were generated for each model at $E_p=10^2$, 10^3 and 10^4 TeV. The lateral distributions are indistinguishable within statistics. For slant depths from 3000 to 5000 hg/cm^2, model III (more inelastic) produces somewhat fewer muons ($\leq$7%) than the standard model I and model II (more elastic) produces somewhat more muons ($\leq$12 %). Intepretation of the sign of this effect is not simple because it results from two competing effects. It has been assumed that the multiplicity distribution remains unchanged as the inelasticity varies. This means that, in the more inelastic model III, each pion in the cascade has higher energy and is therefore less likely to decay. On the other hand, there are more pions with energies high enough to produce a muon above the threshold to reach the detector. The situation could be different in models in which the multiplicity is allowed to increase as the inelasticity increases. In any case, we infer from this test that uncertainties in extrapolation of the inelasticity do not give rise to large uncertainties in the expected properties of underground muons.

F. Diffractive component of the interaction .

The simulation of the hadron-air diffractive interactions were performed by using a model tuned to the $p\bar{p}$ SD interactions. No target effects were included in the model and the same scheme was assumed also for the meson-air interactions. To test the sensitivity of the results to the details of the treatment of diffraction, we have generated showers of selected energies with and without a diffractive component, while keeping the cross sections constant. The differences in lateral distribution and multiplicity are small (less than 5% for $\langle N_\mu \rangle$ and less than 10% for $\langle R_\mu \rangle$). We conclude, therefore, that the treatment of diffraction introduces negligible uncertainty into the model.

G. Primary nucleus fragmentation .

The parametrizations presented above have been obtained in the context of the superposition model : a shower due to a primary of mass A (>1) and energy E is equivalent to A showers generated by A nucleons of energy E/A interacting independently from the top of the atmosphere. If, instead of the superposition model, we treat in a more realistic way the primary nucleus fragmentation, the shower develops somewhat deeper in the atmosphere. As a consequence, the mean number of high energy muons $\langle N_\mu \rangle$ and their mean distance from the shower axis $\langle R_\mu \rangle$ are lower. This effect has been investigated by using a Monte Carlo routine for the nuclear fragmentation[54]. We studied the multiplicity and lateral distributions of muons produced in showers induced by iron nuclei with energy per nucleon E_p between

10 and 10^3 TeV/nucleon and zenith angle θ between 0 and 60 degrees, at depths h between 3000 and 5000 hg/cm^2 :

- the ratio $F_{<N\mu>}$ of the mean number of muons obtained with the fragmentation model to the mean number of muons obtained with the superposition model does not exhibit a clear dependence on E_p, θ and h; the values are all approximately between 0.75 and 0.95 and the mean value is about 0.84 ;
- the ratio $F_{<R\mu>}$ of the mean muon lateral displacement obtained with the fragmentation model to the mean muon lateral displacement obtained with the superposition model is in the range 0.80÷1 even though it does not exhibit a clear dependence on θ and h. However we noticed a slight dependence on the energy per nucleon (for θ and h fixed). We found an average value of 0.84 at 10 TeV/nucleon with a logarithmic increase of about 0.04 per decade of E_p .

We obtained similar effects for the showers induced by alpha particles, so that it is reasonable to assume :

$$F_{<N\mu>} = 0.84 \tag{38}$$

$$F_{<R\mu>} = 0.80 + 0.04 \cdot \log_{10}(E_p/1\ \text{TeV}) \tag{39}$$

independently of the primary mass A (>1). In section VI the effects of these correction factors on the rates of the multiple muon events will be illustrated.

VI. APPLICATIONS

The main features of a muon bundle are the multiplicity and the relative distance between muon pairs (in a bundle with N muons, there are N·(N-1)/2 independent pairs). Figure 15 shows the average values of these quantities, for vertical showers at a fixed slant depth (4000 hg/cm^2) as a function of the primary energy, for proton and iron induced showers. For high primary energy (E>2000 TeV) the multiplicity is much more sensitive to primary mass (for a fixed primary energy) than is the muon lateral spread. For example, above 5000 TeV, the ratio of $<N_\mu>$ for iron compared to proton induced showers is larger than 3, while the average distances between muon pairs do not differ more than 20%. For that reason the multiple muon rates are expected to be the observables more sensitive to the primary composition.

The rate of events with N muons detected can be expressed as :

$$R_N = \sum_A \int dE \cdot \phi_A(E) \cdot P_N(E,A) = \sum_A \int dE \cdot S_N(E,A) \tag{40}$$

Here $\phi_A(E)$ represents the differential flux of nuclei of mass A, at energy E, according to a given composition model (see Eq.41 below). The function P_N represents an acceptance for the detection of N muons due to a primary of mass A and energy E. This function does not depend on the composition model. It depends on the shower development (through the muon

multiplicity and lateral spread), on the shape of the mountain above the laboratory (through a function $h(\theta,\phi)$ which associates a given rock thickness to a given primary direction (θ,ϕ)), on the rock properties (through the rock density and through a function which converts the actual rock thickness into a standard rock thickness[55]), on the detector geometry and efficiency and on the track reconstruction capability. Some examples of P_N functions for N=1, 6 and 16 are shown in Fig. 16. Once the function P_N has been calculated for a given set of (A, E) values, the rate of events with N muons, for a given composition model, can be obtained first by multiplying $P_N(A, E)$ by $\phi_A(E)$ (the model dependent function S_N is obtained), then integrating over the primary energy E and finally summing over the five mass components. All these steps of the calculation are very fast (a few seconds), so that an arbitrary number of different composition models can be checked for comparison with data.

The only time consuming operation is the calculation of $P_N(A, E)$. It can be realised in two ways:

- the event generation :
  this is a Monte Carlo approach in which samples of events are generated (for fixed values of mass A and energy E) directly from the parametrizations and folded into the detector. In this case all details of the detector can be applied event-by-event (on the assumption that the small fraction of stopping muons is neglected). This calculation procedure requires much work because it is a multistep one: first, the muons are generated relative to the shower axis; then the axis position relative to the detector is sampled and the event is folded into the detector; the simulated raw data produced are recorded on a file which is the input of a routine for the track reconstruction and the histogramming;
- the numerical integration :
  alternatively, one can use the parametrizations as the basis of a numerical integration to obtain $P_N(A, E)$ for a set of values of A and E. The latter option is much faster but requires one to assume that for a given muon direction one can calculate an area inside which the probability of detection (and reconstruction) of the associated track is 1, independently of the presence of other muons in the event. This calculation technique was already applied to the analysis of the NUSEX data[4], in which the detector was considered as a box and a minimum vertical track length was assumed for the detection and reconstruction of each track. This possibility relied on the fact that the NUSEX detector is constituted of a large number (134) of horizontal streamer tubes so that one can define a minimum vertical track length for which the detection efficiency is almost 1; furthermore, the tracks reconstructed in the two orthogonal views can be associated so that the number of planes crossed by each track is known and a comparison with the calculation is possible. A complete description of the numerical integration technique can be found in Ref. 56.

Another procedure sometimes used for the calculation of the multiple muon rates R_N, is to sample the mass and the energy within a series of energy bands according to a given composition model. As a consequence of the spectrum steepness, the primary energy has to be sampled separately from several bands; for example, at Gran Sasso the bands could be : from 2 to 10 TeV, from 10 to 10^2 TeV,...., from 10^5 to 10^6 TeV. In this case the number of steps in the calculation is reduced; instead of a run for each mass A and energy E, the generation for a

given composition model requires just one run for each energy band. However, in this case, the result of the calculation is not the function $P_N(A, E)$, but its integrals over the bands already weighed with the flux $\phi_A(E)$. Thus, in this case the whole calculation has to be repeated for any model that one wants to check.

Whichever procedure is used, it is helpful to know which are the important energies and masses for the integral in Eq.40. We will therefore display the integrand $S_N(A, E)$ as a function of E and A in figures 21-23 below, after we have discussed a range of composition models.

In the following, we report the results of the calculation of rates of multiple, coincident muons in a simplified version of the MACRO detector[57]. Rather than attempting to simulate the real detector, we have represented a single "supermodule" as a box of 12x12x5 m^3, requiring a minimum vertical track length of 2 m for each track to be detected and reconstructed. This simplification is necessary for applying the numerical integration technique described above. Even though it is not adequate for interpretation of real data, for which it will be necessary to simulate in detail the response of the actual detector, it is sufficient, however, to illustrate the sensitivity of a detector of this general size and location to the elemental composition of the primary cosmic rays. We give examples both for a single "supermodule" (hereafter indicated as SM) and for six "supermodules" (72x12x5 m^3).

We compare the rates of single and multiple muons for four representative compositions in the literature. These same models were used in the analysis of Ref.4. In each case the cosmic ray nuclei are treated as five groups of mass (average mass : A=1 for protons, A=4 for alphas, A=14 for the CNO group, A=28 for the Mg-Si group and A=56 for the Fe group). The differential flux for each mass component has been expressed through a power-law :

$$\phi_A(E) = K \cdot (E/1\ \text{GeV})^{-\gamma} \qquad (41)$$

where ϕ_A and K are in nuclei/($m^2 \cdot s \cdot sr \cdot$GeV/nucleus). For energy E bigger than a cutoff value E_c, the slope changes; it is indicated as $\gamma(E>E_c)$ in table III. This table[4] lists the values of the parameters (normalization constants, slopes and cutoff energies) of the four models we consider:

- p-poor model (PP) :
  this cosmic ray composition[58] is inferred from the intensities of γ families observed both at Mt. Kanbala and at Mt. Fuji. Its main distinctive features are a low value of the proton cutoff ($E_c=10^5$ GeV) and a big increase of the ratio iron/proton (see Fig.17a) ;
- Maryland model (MD) :
  this model[59] provides steep proton and α spectra and a big relative increase of Mg-Si and iron fluxes (see Fig.17b) ;
- Constant Mass Composition model (CMC) :
  In the CMC model all the mass groups have the same spectral slope so that the increase of the heavy nuclei percentage is uniquely due to the rigidity dependent steepening (see Fig.17c). The version used here is based on the analysis of Kempa and Wdowczyk[60] of the hadron

intensities at mountain altitudes, and differs only in the use of γ=2.71 rather than γ=2.70 below the rigidity cutoff.

- Linsley model (LI) :
  in the model suggested by Linsley[61], the existence of a new proton source is assumed. This source takes over at high energy and cancels the effect of the conventional proton bend. As a consequence, the proton percentage increases with energy (see Fig.17d).

In all cases (except for protons in the Linsley model) all components are assumed to steepen at the same magnetic rigidity. We stress that in some cases there are several versions of the same basic model in the literature. For the sake of definiteness, we use here versions identical to those used in Ref.4. In principle, all the models should reproduce the all-particle spectrum measured in air shower experiments. However, these measurements are affected by considerable uncertainties and the procedure to convert the measured shower size into the primary energy depends on many hypotheses concerning the shower development. Thus, although the all-particle spectra provided by these four models (Fig.18) are rather different, they are all consistent with the primary spectra obtained from the measured electron and muon size distributions. While the differences are of the order of 20÷30% at 10^3 GeV, at the energies around and over the bending point they become considerable; for example the PP and LI predictions differ by more than a factor 2 at 10^7 GeV.

The muon rates for one SM for each of the compositions are shown in Table IV. The rates of single muons are not identical in the four models and differ up to about 40% for the two extreme models Maryland (heavy) and Linsley (light). This is primarily a consequence of the fact that these models correspond to somewhat different primary nucleon spectra around 10÷100 TeV. However, the calculation of the rates reported in Table IV is affected by systematical uncertainties. Those related to the description of the mountain topography and rock density can be partially suppressed by considering the ratio of multiples to singles (Table V).

It is useful to show some characteristic distributions for the extreme models, Maryland and Linsley , for a single SM. Figure 19 shows the ratio R_N/R_1 of multiples to singles for these models. We notice that in the ratio R_{16}/R_1 there is about a factor 3 between the two models. Figure 20a) shows the mean primary energy per nucleus that gives rise to events of various multiplicities. They are rather similar in the two models, although, as expected, the mean primary energy is somewhat higher for the high multiples in the model with mostly protons. In contrast, the mass of the progenitors of the underground events (Fig. 20b) is quite different in the two models. For example, the events with 6 muons are mostly (>50%) due to primary protons for the Linsley model, while the proton contribution according to the Maryland model is only about 2%. Figures 21, 22 and 23 illustrate these differences graphically, by showing the relative contributions of the five nuclear groups in these two models to the rates of singles, 6–fold and 16–fold events.

Apart from increased counting rate, there is little qualitative difference between the results for six SM's (see Table VI) as compared to those with one SM. In Table VII we report

the ratios of multiples to singles for each model. Figure 24 shows the ratio between the rates R_N(6 SM) obtained with six SM's and the rates R_N(1 SM) obtained with one SM, as a function of the muon multiplicity N. We notice that, while the ratio of singles is lower than 6 (which is the ratio of the top areas between the cases 6 SM's and 1 SM), for higher multiplicities R_N(6 SM)/R_N(1 SM) is bigger than 6. This can be explained as follows : the rate for a given multiplicity N of muons detected is obtained by summing over the multiplicity $N_a \geq N$ of muons at the detection level weighing with the probability $P(N_a, N)$ that only N of the N_a muons are detected. In the limit of a detector of infinite area, the matrix P is diagonal $P(N_a, N)=1$ for $N_a=N$ and $P=0$ for $N_a \neq N$ so that there is no contribution from the multiplicities $N_a>N$. Generally speaking, the smaller is the detector, the bigger is the relative contribution of the multiplicities $N_a>N$. This consideration explains also the results of figure 25, where the ratios R_N/R_1 of multiples to singles obtained with one SM and six SM's (for the CMC composition model) are compared. As a consequence of the larger relative contribution to the multiplicity N of the multiplicities $N_a>N$ for the smaller detector, the mean primary energy associated with a given multiplicity N and with a given composition model is greater for one SM than for six SM's (Fig.26).

The differences between the predictions in tables IV-VII should be compared with the systematical uncertainties in the calculation. One of the biggest sources of uncertainty is the treatment of the nuclear fragmentation for showers induced by primaries with mass > 1. In a simplified treatment of the problem, the fragmentation effects can be accounted for by multiplying the values of $\langle N_\mu \rangle$ and $\langle R_\mu \rangle$ obtained from the parametrizations by some correction factors, $F_{\langle N\mu \rangle}$ and $F_{\langle R\mu \rangle}$ respectively (Eqs. 39 and 40). In figure 27 we show the ratio of the rates with fragmentation effects to the rates presented previously in Table IV (associated with the "superposition model"). We notice that the differences between the rates are quite considerable (10÷20%) for high (≥6) multiplicity events. Indeed, they can be large compared to the differences between rates in models such as p-poor and CMC which are rather different (see table III and compare Figs.17a and 17c). For example, the rates of 9-muon events in Table IV differ less than 20% between the various models (except for Maryland), so that, in principle, the uncertainties in the calculation do not allow one to discriminate between the different models except for the most extreme case. On the other hand, we notice differences also in the rates of single muons in Table IV. These depend mainly on the flux of protons of energy 1÷100 TeV. Since the hadronic interactions are rather well known in this energy range and the uncertainties in the nuclear fragmentation do not affect the proton showers, the rate of single muons can be useful to discriminate models which assume an extreme hypothesis on the proton flux at these energies. The total uncertainty introduced into the calculation by all the other effects discussed in Section V is comparable to the uncertainty from the treatment of fragmentation.

A general problem with making inferences about primary composition from rates of multiple muon events deep underground is that the normalization of the all-particle spectrum is poorly known. As an example, the predicted rates of high multiplicity events (>10) differ by about a factor 2 for the two extreme models considered in this paper. The heavy composition

(MD) has about twice the rate of high multiplicity events as the proton rich model (LI). On the other hand, Auriemma et al.[62] found a factor of about 4 of difference between a similar pair of heavy and proton rich models. The two results are in fact consistent. Auriemma et al. required that both composition models give the same all-particle spectrum. In contrast, the LI spectrum used here is about a factor 2 higher than the MD spectrum in the relevant energy range around 10^7 GeV (see figures 18 and 20a), thus reducing the difference between the rates of high multiplicity events in the two models. In general, we note from Fig.18 that the models with a larger fraction of protons have the largest flux of particles at high energy. Thus there is a tendency in primary flux models discussed here to compensate a low probability per proton of obtaining large N_μ with a large flux of high energy protons. Further work is needed to impose an appropriate self consistency criterion on various trial composition models. Requiring the same all-particle spectrum[62] was an attempt in this direction, but it may not be sufficient because the relations between primary energy and measured quantities such as N_μ and N_e in air showers depend on composition.

Observation of events by the surface EAS-TOP array in coincidence with the underground detector[1] can provide complementary information about the composition[63,64]. In particular, composition models with a large fraction of protons will give significantly larger surface showers for events of high multiplicity than composition models with a large fraction of heavy nuclei. There are two reasons for this : (i) to get an event with many muons from a primary proton requires higher energy than from a primary heavy nucleus, and therefore a larger shower; (ii) not only are the proton showers larger, but they also do not die out as fast as the nuclear showers. For both reasons, therefore, surface showers associated with events of high multiplicity underground will have characteristically different size distributions for heavy and light compositions. This distinction will be independent of normalization in first order because it concerns the shape of the associated size distribution at the surface rather than the rate alone.

Finally, we note that measurements of lateral spread in muon bundles and study of rates as a function of direction and slant depth will allow the calculations to be tuned and should improve the ability to discriminate among various models of composition.

REFERENCES

1) EAS-TOP Coll. and MACRO Coll., Proc. 21st ICRC (Adelaide), Vol.9, p.331 and p.335 (1990).
2) J.A. Wrotniak, SHOWERSIM/84, Univ. of Maryland Report p.85-191 (unpublished).
3) T.K. Gaisser and Todor Stanev, Nucl. Instr. and Meth. A235, 183 (1985).
4) M. Aglietta et al., Nucl. Phys. (Proc. Suppl.) B14, 193 (1990).
5) T.K. Gaisser, U.P. Sukhatme, G.B. Yodh, Phys. Rev. D 36, 1350 (1987).
6) J.W. Elbert et al., Phys.Rev. D12, 660 (1975).
7) L. Durand and H. Pi, Phys. Rev. D 40, 1436 (1989).
8) Carlo Forti, Tesi di Laurea, Universita` di Roma I, Aprile 1988.
9) A. Giovannini and L. Van Hove, CERN-TH/87-4894.
10) UA5 Collaboration, G.J.Alner et al., CERN-EP/86-213.
11) UA5 Collaboration, G.J.Alner et al., Phys. Lett. 160B, 199 (1985), and 167B, 476 (1986).
12) M. Antinucci et al., Lettere al Nuovo Cimento, Vol.6, n.4, 121 (1973).
13) J. Engler et al., Nucl. Phys. B84, 70 (1975).
14) AFS Collaboration, Akesson et al., Nucl. Phys. B203, 27 (1982).
15) UA5 Collaboration, G.J. Alner et al., Nucl. Phys. B258, 505 (1985).
16) S. Uhlig et al., Nucl. Phys. B132, 15 (1978).
17) UA1 Collaboration, F. Ceradini, Proc. Int. Europhysics Conference on High Energy Physics (Bari), 363 (1985).
18) UA1 Collaboration, G. Arnison et al., Phys. Lett. 118B, 167 (1982).
19) M. Basile et al., Lettere al Nuovo Cimento, Vol.38, n.10, 359 (1983).
20) S. Jadach, Computer Physics Communications, Vol.9, 297 (1975).
21) W. Thome' et al., Nucl. Phys. B129, 365 (1977).
22) UA5 Collaboration, G.J. Alner et al., Zeit. fur Physik C33, 1 (1986).
23) UA5 Collaboration, G.J. Alner et al., Phys. Lett. 160 B, 193 (1985).
24) UA5 Collaboration, G.J. Alner et al., Phys. Rep. 154, 247 (1987).
25) L. Voyvodic, Proc. Workshop on Cosmic Ray Interactions, La Paz, July 1982, p.258.
26) T. Aziz, Int. J. Mod. Phys.A, Vol.1, n.4, 991 (1986).
27) F. Dengler et al., Z. Phys. C33, 187 (1986).
28) L.W. Jones, Proc. Workshop on Cosmic Ray Interactions, La Paz, July 1982, p.1.
29) J.W. Cronin et al., Phys. Rev. D11, 3105 (1975).
30) UA5 Collaboration, G.J. Alner et al., CERN-EP/86-126.
31) D.S. Barton et al., Phys. Rev. D27, 2580 (1983).
32) G. Giacomelli and M. Jacob, Phys. Rep. 55, 1 (1979).
33) UA4 Collaboration, CERN-EP/85-154.
34) M.G. Albrow et al., Nucl. Phys. B108, 1 (1976).
35) UA4 Collaboration, M. Bozzo et al., Phys. Lett. 136B, 217 (1984).
36) K. Goulianos, Phys. Rep. 101, 169 (1983).
37) UA4 Collaboration, D. Bernard et al., Phys. Lett. 166B, 459 (1986).
38) The experimental results of the collaboration Pisa-Stony Brook at ISR (G. Bellettini, AIP Conference Proc. n.15, High Energy collisions, Stony Brook 1973, p.9) could be

interpreted with an isotropic decay model which gives a rapidity distribution of width independent of the mass M of the diffractive cluster.

39) K. Greisen, Progress in Cosmic Ray Physics, Vol.III, 1 (1956). For more details see also Ref.64.
40) H. Bilokon et al., Proc. 20th ICRC (Moscow), Vol.9, p.199 (1987).
41) R.M. Sternheimer and R.F. Peierls, Phys. Rev. B3, 3681 (1971).
42) R.P. Kokoulin and A.A. Petrukhin, Proc. 12th ICRC (Hobart), Vol. 6, p.2436 (1971).
43) A.A. Petrukhin and V.V. Shestakov, Can. J. Phys. Vol.46, S377 (1968).
44) Y. Minorikawa et al., Nuovo Cimento C, Vol. 4, 471 (1981).
45) V.L. Highland, Nucl. Instr. and Meth. Vol. 129, 497 (1975).
46) B. Rossi, "High Energy Particles", Prentice Hall Englewood Cliffs, New Jersey (1952).
47) M. Calicchio et al., Phys. Lett. 193B, 131 (1987).
48) B. d'Ettorre Piazzoli, "Observation of Muons from Cygnus X-3 in the NUSEX experiment", Proc. 19th ICRC (La Jolla), Vol.9, p.455 (1985).
49) J.W. Elbert, Proc. DUMAND Summer Workshop (ed.A. Roberts), Vol.2, p.101 (1978).
50) J.W. Elbert et al., Phys. Rev. D27, 1448 (1983).
51) C. Castagnoli et al., Nuovo Cimento 82A, 78 (1984).
52) J.N. Capdevielle and J. Gawin, Proc. 19th ICRC (La Jolla), Vol.7, p.20 and p.24 (1985).
53) B.Z. Kopeliovich, N.N. Nikolaev and I.K. Potashnikova, Phys. Rev. D 39, 769 (1989), and T.K. Gaisser and Todor Stanev, Phys. Lett. 219 B, 375 (1989).
54) T.K. Gaisser and Todor Stanev, Bartol Research Foundation of the Franklin Institute, Report BA-82-1; T.K. Gaisser, Todor Stanev, P.Freier and C.J. Waddington, Phys. Rev. D25, 2341 (1982).
55) A.G. Wright, Proc. 13th ICRC (Denver), Vol.3, p.1709 (1973).
56) G. Bologna et al., Nucl. Instr. and Meth. A234, 581 (1985).
57) MACRO Collaboration, Proc. 21st ICRC (Adelaide), Vol.9, p.356 (1990).
58) R. Ren et al., Phys. Rev. D38, 1404 (1988). The p-poor composition is called HD here.
59) G.B. Yodh, T.K. Gaisser and T. Stanev, Proc. of ICOBAN 84 (Park City, Utah, edited by D. Cline) p.300. See also G.B. Yodh et al., Phys. Rev. D29, 892 (1984).
60) J. Kempa and J. Wdowczyk, Jour. Phys. G : Nucl.Phys., Vol.9, 1271 (1983).
61) J. Linsley, Proc. 18th ICRC (Bangalore), Vol.12, p.135 (1983). See also C. Fitchel and J. Linsley, Ap. J., Vol.300, 474 (1986).
62) G. Auriemma et al., Proc. 21st ICRC (Adelaide), Vol.9, p.362 (1990).
63) T.K. Gaisser et al., Proc. 21st ICRC (Adelaide), Vol.9, p.323 (1990).
64) H. Bilokon et al., Proc. 21st ICRC (Adelaide), Vol.9, p.114 (1990). This paper discusses the anticorrelation between N_μ and N_e for a given primary energy and mass, which must be accounted for in analysis of surface-underground coincidences.

TABLE I - Mean number of muons above 500 GeV at production, generated in proton showers of energy E_p (TeV) at zenith angle 28°.

E_p (TeV)	10	10^2	10^3	10^4	10^5
$<N_\mu>$	.299	2.31	12.5	71.6	436

TABLE II - Mean inelasticity for the process p+air—>N+anything, at different lab-energies E_{lab}, according to the three interaction models considered in the text. Model I is preferred.

E_{lab} (TeV)	10^2	10^3	10^4
Model I	0.61	0.58	0.57
Model II	0.54	0.51	0.50
Model III	0.68	0.65	0.65

TABLE III - Normalization factor K ($m^{-2}\cdot s^{-1}\cdot sr^{-1}\cdot(GeV/nucleus)^{-1}$), slope, cutoff energy E_c (GeV) and slope after cutoff for the four models considered in the text.

GROUP	K	γ	E_c	γ(E>E_c)
P-poor composition				
p	$1.51\ 10^4$	2.70	$1.0\ 10^5$	3.0
α	$7.02\ 10^3$	2.70	$2.0\ 10^5$	3.0
CNO	$2.68\ 10^3$	2.61	$7.0\ 10^5$	3.0
Mg	$2.93\ 10^3$	2.62	$1.4\ 10^6$	3.0
Fe	$8.56\ 10^2$	2.50	$2.8\ 10^6$	3.0
Maryland composition				
p	$1.98\ 10^4$	2.75	$3.0\ 10^5$	3.35
α	$1.03\ 10^4$	2.77	$6.0\ 10^5$	3.37
CNO	$2.15\ 10^3$	2.60	$2.1\ 10^6$	3.20
Mg	$1.14\ 10^3$	2.50	$4.2\ 10^6$	3.10
Fe	$5.95\ 10^2$	2.50	$8.4\ 10^6$	3.10
Constant mass composition				
p	$1.72\ 10^4$	2.71	$2.0\ 10^6$	3.00
α	$9.20\ 10^3$	2.71	$4.0\ 10^6$	3.00
CNO	$6.20\ 10^3$	2.71	$1.4\ 10^7$	3.00
Mg	$9.20\ 10^3$	2.71	$2.6\ 10^7$	3.00
Fe	$6.20\ 10^3$	2.71	$5.2\ 10^7$	3.00
Linsley composition				
p	$2.60\ 10^4$	2.73	$1.0\ 10^5$	
	$1.84\ 10^3$	2.50	$1.0\ 10^7$	3.02
α	$8.16\ 10^3$	2.73	$1.0\ 10^6$	3.23
CNO	$5.65\ 10^3$	2.73	$3.5\ 10^6$	3.23
Mg	$7.30\ 10^3$	2.73	$7.0\ 10^6$	3.23
Fe	$6.33\ 10^3$	2.73	$1.3\ 10^7$	3.23

TABLE IV - Underground muon rates for six different multiplicities N_μ in one SM, according to the four composition models considered in the text. Units are events/year.

N_μ	1	3	6	9	12	16
PP	$1.15 \cdot 10^6$	$5.56 \cdot 10^3$	$4.29 \cdot 10^2$	106	37.7	13.9
MD	$9.55 \cdot 10^5$	$6.06 \cdot 10^3$	$5.83 \cdot 10^2$	155	56.9	21.1
CMC	$1.20 \cdot 10^6$	$5.69 \cdot 10^3$	$4.01 \cdot 10^2$	97.0	35.5	13.4
LI	$1.37 \cdot 10^6$	$6.07 \cdot 10^3$	$3.98 \cdot 10^2$	88.8	29.7	9.97

TABLE V - Ratio of multiples to singles R_N/R_1 for five different multiplicities N in one SM, according to the four composition models considered in the text.

	R_3/R_1	R_6/R_1	R_9/R_1	R_{12}/R_1	R_{16}/R_1
PP	$4.82 \cdot 10^{-3}$	$3.72 \cdot 10^{-4}$	$9.16 \cdot 10^{-5}$	$3.27 \cdot 10^{-5}$	$1.20 \cdot 10^{-5}$
MD	$6.35 \cdot 10^{-3}$	$6.10 \cdot 10^{-4}$	$1.63 \cdot 10^{-4}$	$5.96 \cdot 10^{-5}$	$2.21 \cdot 10^{-5}$
CMC	$4.75 \cdot 10^{-3}$	$3.43 \cdot 10^{-4}$	$8.09 \cdot 10^{-5}$	$2.96 \cdot 10^{-5}$	$1.12 \cdot 10^{-5}$
LI	$4.44 \cdot 10^{-3}$	$2.91 \cdot 10^{-4}$	$6.48 \cdot 10^{-5}$	$2.17 \cdot 10^{-5}$	$7.28 \cdot 10^{-6}$

TABLE VI - Underground muon rates for four different multiplicities N_μ in six SM's, according to the four composition models considered in the text. Units are events/year.

N_μ	1	3	6	16
PP	$6.06 \cdot 10^6$	$4.16 \cdot 10^4$	$3.44 \cdot 10^3$	115
MD	$4.99 \cdot 10^6$	$4.34 \cdot 10^4$	$4.46 \cdot 10^3$	175
CMC	$6.29 \cdot 10^6$	$4.16 \cdot 10^4$	$3.04 \cdot 10^3$	102
LI	$7.20 \cdot 10^6$	$4.29 \cdot 10^4$	$2.90 \cdot 10^3$	78.8

TABLE VII - Ratio of multiples to singles R_N/R_1 for three different multiplicities N in six SM's, according to the four composition models considered in the text.

	R_3/R_1	R_6/R_1	R_{16}/R_1
PP	$6.87 \cdot 10^{-3}$	$5.67 \cdot 10^{-4}$	$1.89 \cdot 10^{-5}$
MD	$8.69 \cdot 10^{-3}$	$8.93 \cdot 10^{-4}$	$3.51 \cdot 10^{-5}$
CMC	$6.61 \cdot 10^{-3}$	$4.83 \cdot 10^{-4}$	$1.61 \cdot 10^{-5}$
LI	$5.96 \cdot 10^{-3}$	$4.03 \cdot 10^{-4}$	$1.09 \cdot 10^{-5}$

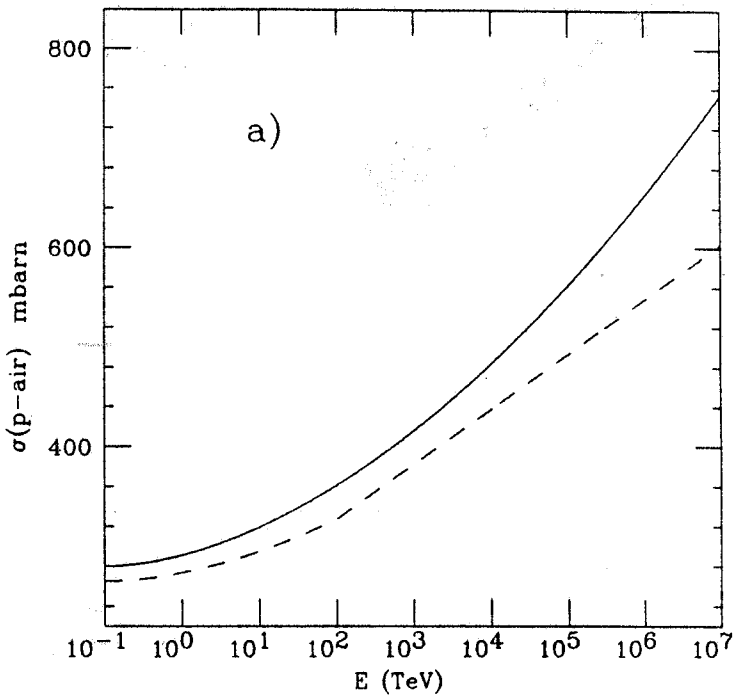

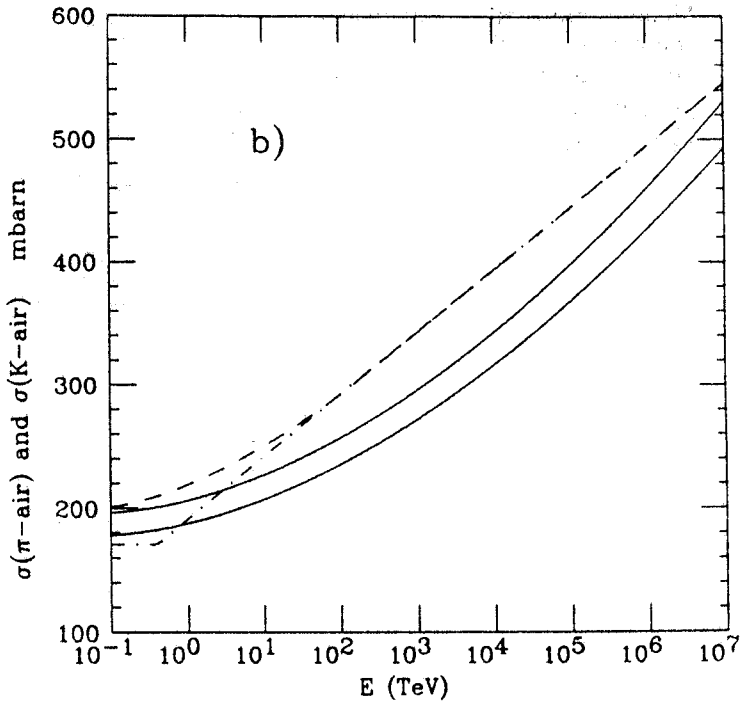

FIG. 1 - Cross sections for hadrons on air as a function of the incident energy E. Solid lines - ref.6; dashed lines - see text. **a)** proton-air. **b)** upper curves : π-air; lower curves : K-air.

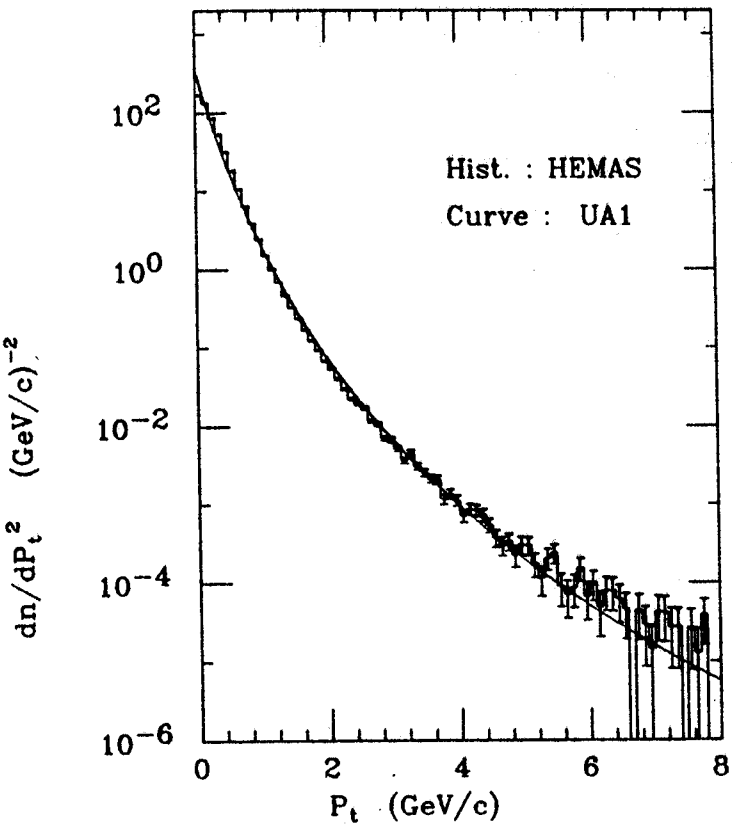

FIG. 2 - Transverse momentum distribution for charged particles with $|y|<2.5$, in $p\bar{p}$ N S D interactions at $\sqrt{s}$=546 GeV. The Monte Carlo result (histogram with statistical errors) is compared to a fit of the UA1 data[18].

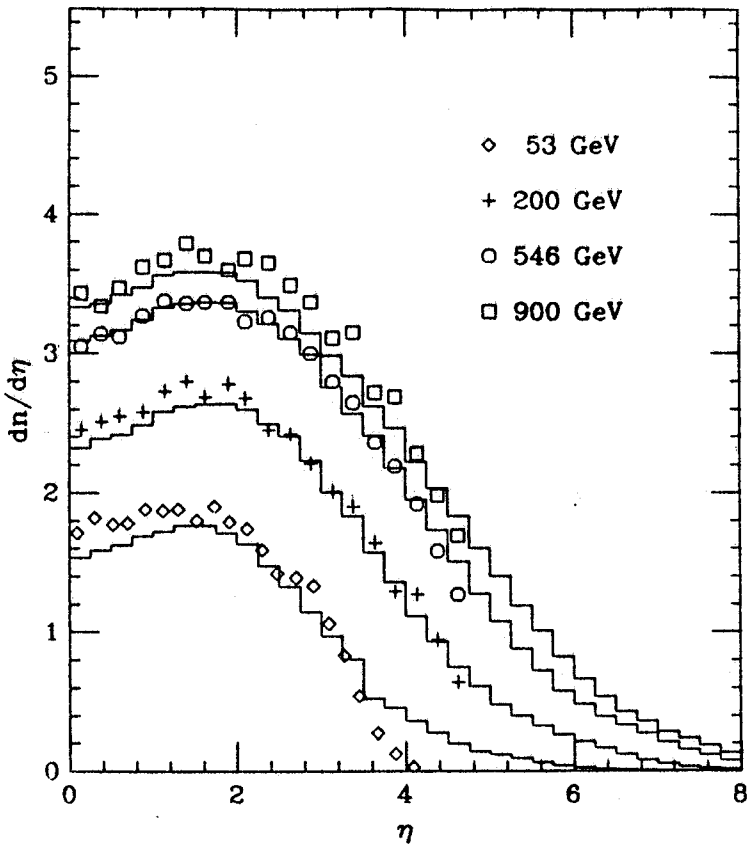

FIG. 3 - Inclusive pseudorapidity distributions of charged particles. The Monte Carlo results (histograms) are compared to data for pp NSD interactions[21] at $\sqrt{s}$=53 GeV and for $p\bar{p}$ NSD interactions[22] at $\sqrt{s}$=200, 546 and 900 GeV.

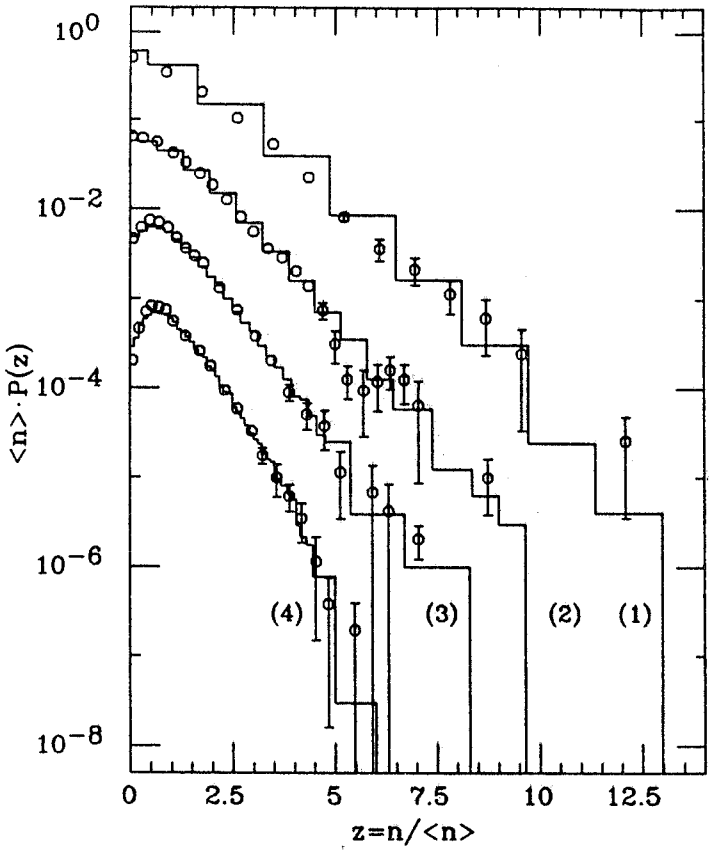

FIG. 4 - Charged multiplicity distributions in $p\bar{p}$ NSD interactions at $\sqrt{s}$=546 GeV in the regions $|\eta| < 0.2$ (1), 0.5 (2), 1.5 (3) and 3.0 (4) plotted as $\langle n \rangle \cdot P(z)$ vs. $z=n/\langle n \rangle$. The Monte Carlo results (histograms) are compared with UA5 data[23] (open circles). The vertical scale has to be multiplied by a factor: 10^3 for $|\eta| < 3.0$, 10^2 for $|\eta| < 1.5$, 10^1 for $|\eta| < 0.5$, 1 for $|\eta| < 0.2$.

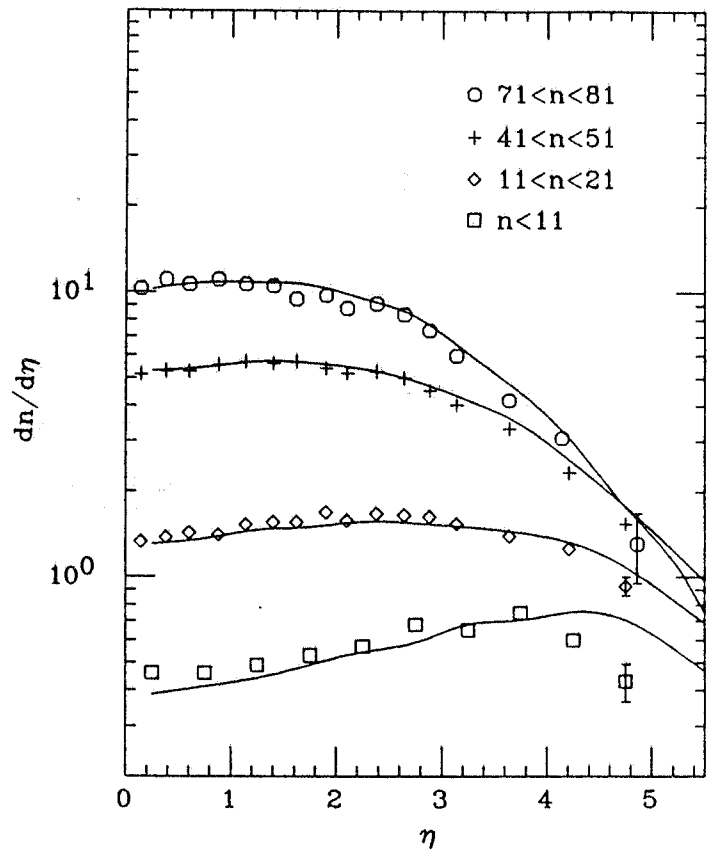

FIG. 5 - Pseudorapidity distributions of charged particles in four charged multiplicity windows for $p\bar{p}$ NSD interactions at $\sqrt{s}$=546 GeV. The Monte Carlo results (curves) are compared to UA5 data[24].

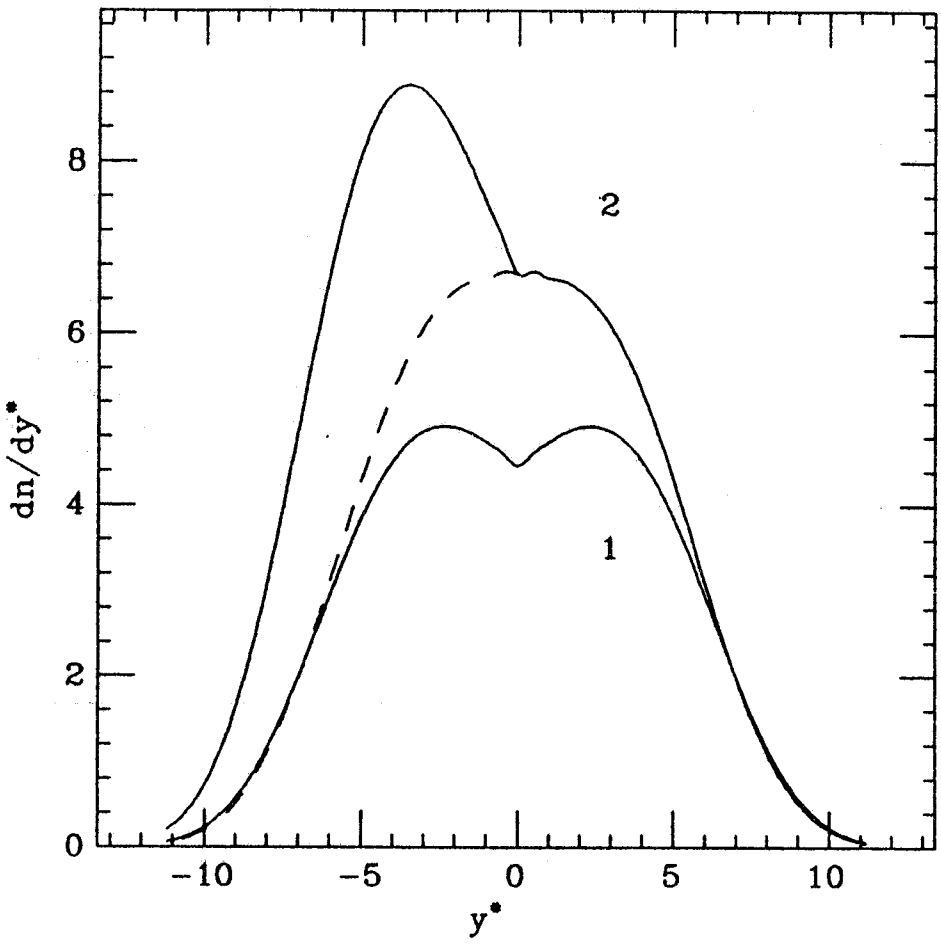

FIG. 6 - Inclusive rapidity distributions (in the projectile-target nucleon C.M.) for charged particles produced in pp (curve 1) and in p-air (curve 2) non diffractive interactions at $\sqrt{s}$=10 TeV, calculated using the functions $F(\xi)$ and $R(z)$ (see text). In our algorithm, the backward particles between the curve 2 and the dashed curve are not produced.

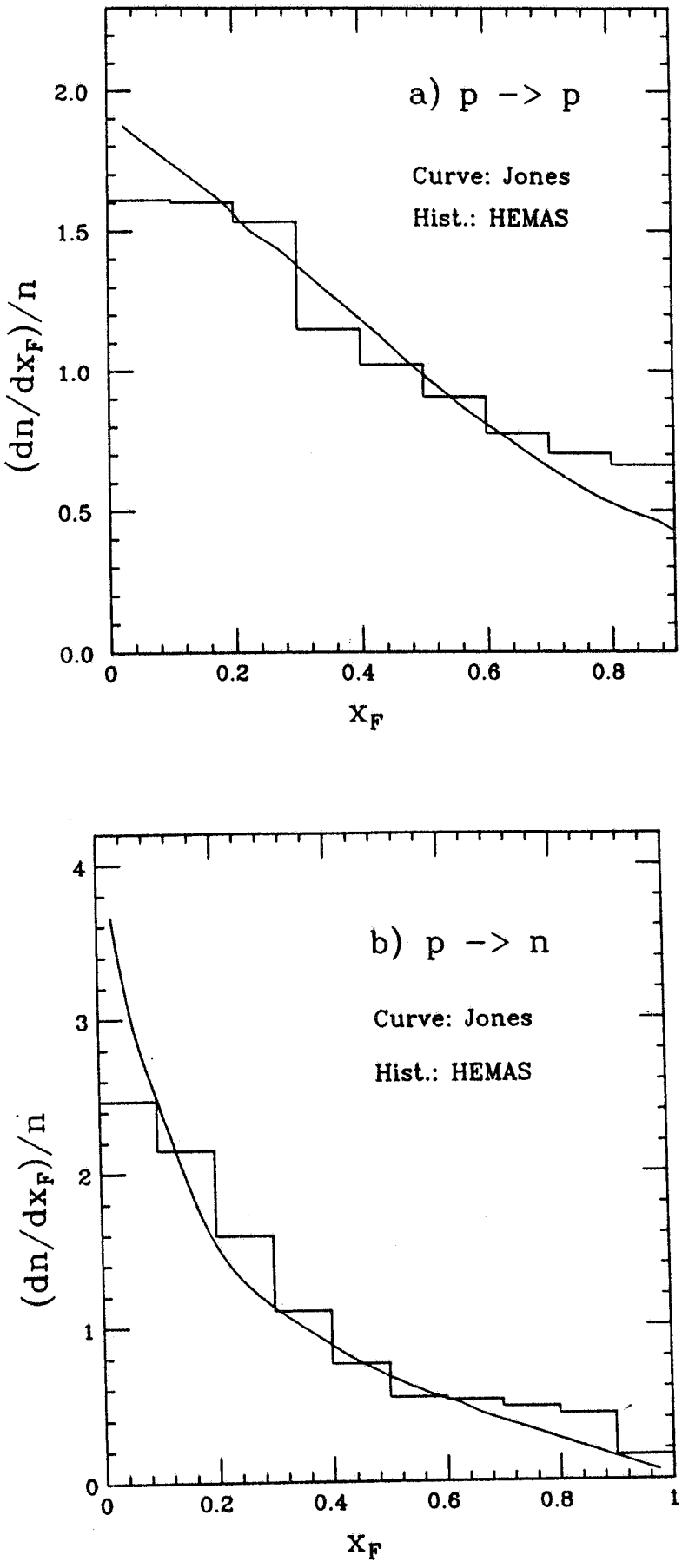

FIG. 7 - x_F distribution of the leading nucleon in fixed target interactions. **a)** the Monte Carlo result (histogram) for the p+air→p+anything is compared to data (continuous curve) at lab energy 100 GeV for p+Carbon→ p+anything, quoted by Jones[28]. **b)** the Monte Carlo result (histogram) for p+air→ n+anything is compared to data (continuous curve) at lab energy 300 GeV for p+Be→ n+anything quoted by Jones. Each distribution is normalized to unit area.

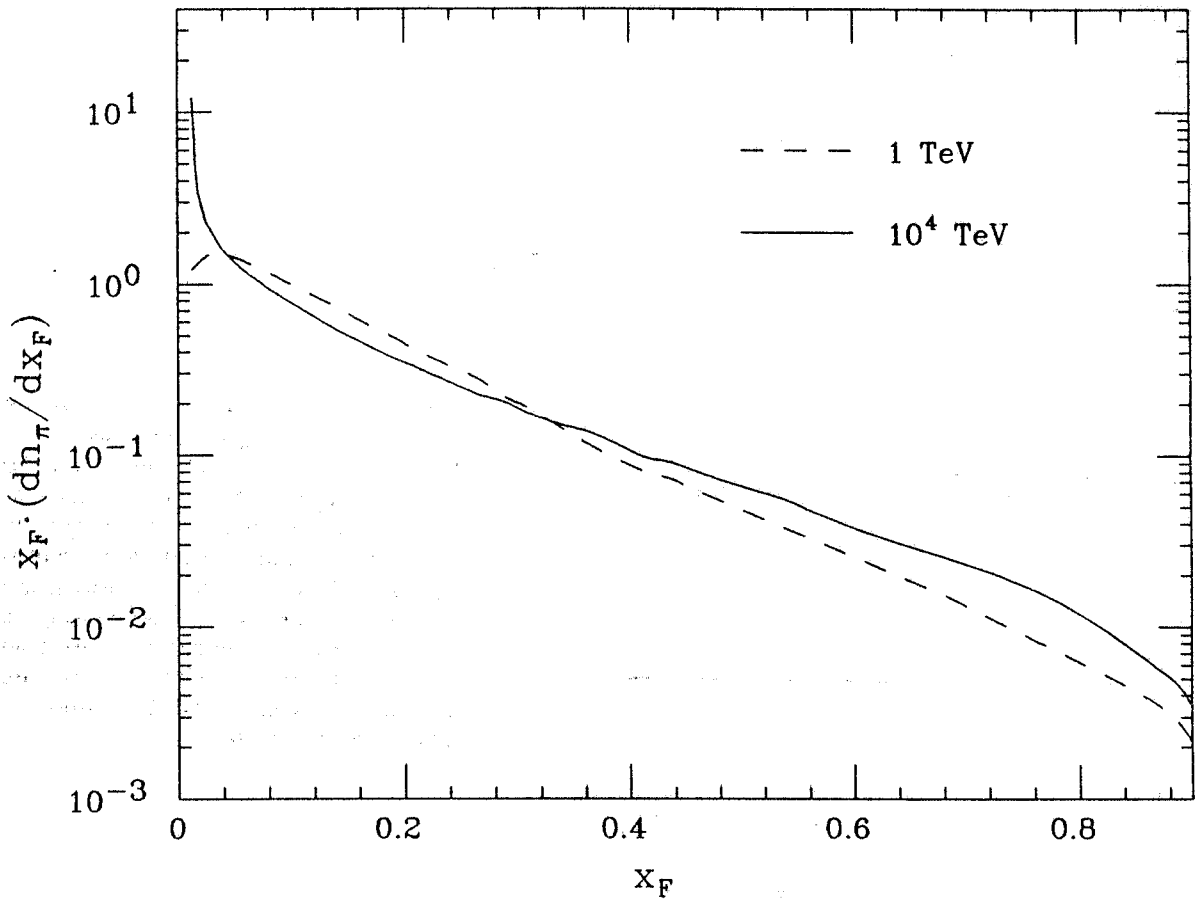

FIG. 8 - Inclusive x_F distributions of charged pions produced by our model in 10^5 p-air non diffractive interactions at lab energy 1 TeV (dashed curve) and at lab energy 10^4 TeV (continuous curve).

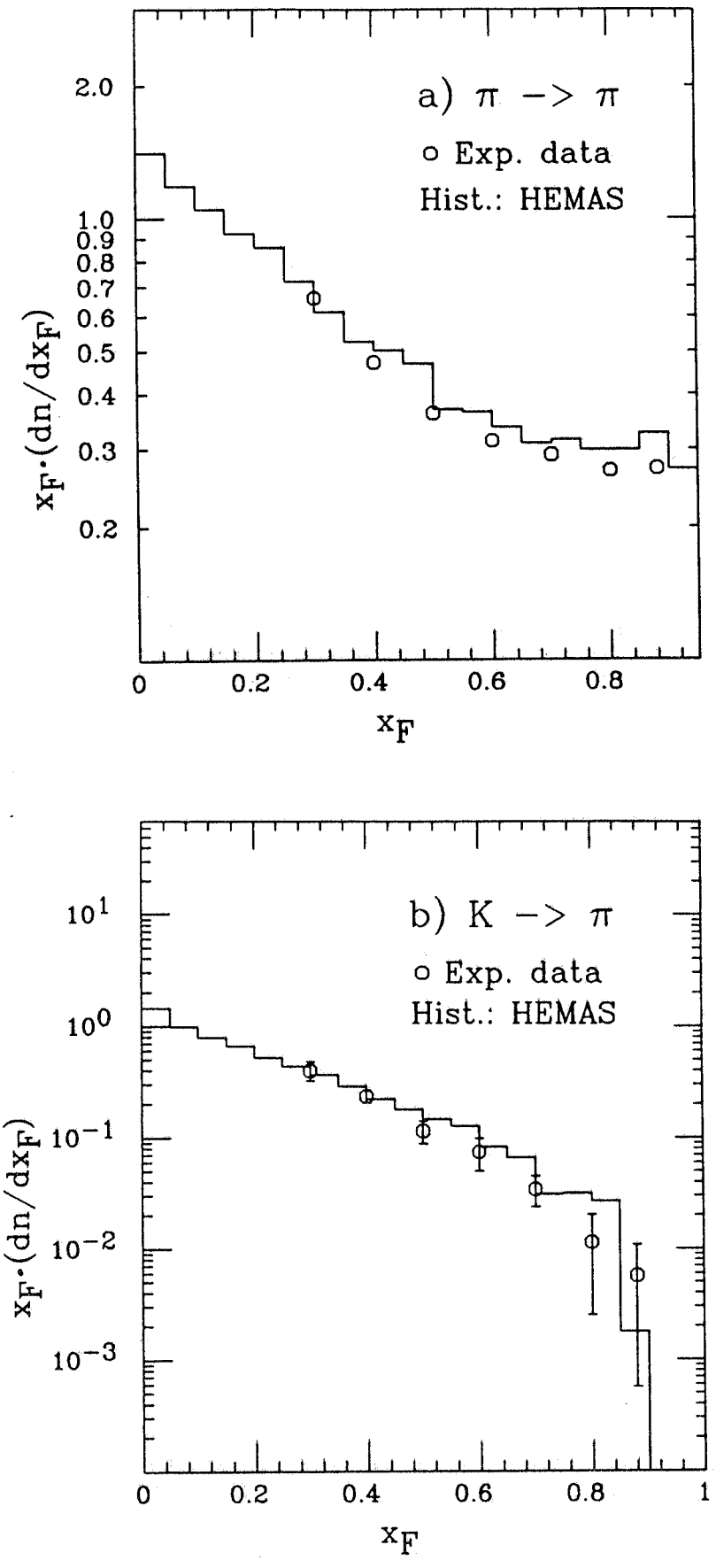

FIG. 9 - x_F distributions of final charged pions in meson interactions on fixed target at lab energy 100 GeV. a) the Monte Carlo result (histogram) for π^++air—> $\pi^\pm$+anything is compared to data (o) from Barton et al.[31] with a Carbon target. The data are normalized so as to coincide with the Monte Carlo in x_F=0.3.
In b) the same as in a) for K^++air—>$\pi^\pm$+anything.

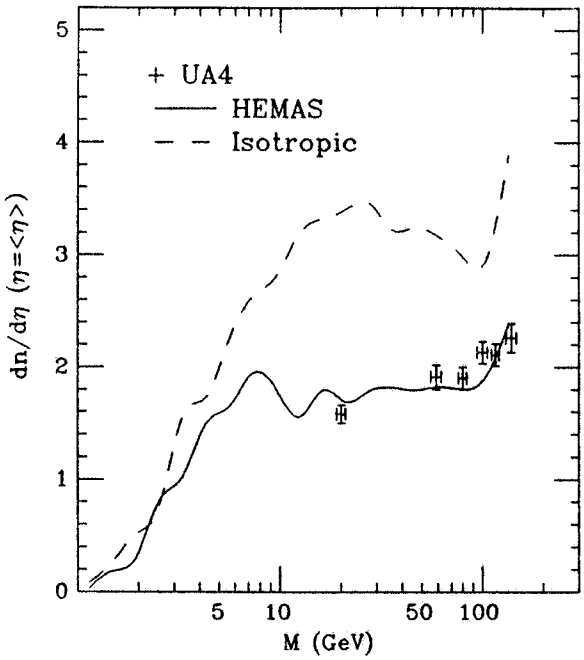

FIG. 10 - Charged particle density in pseudorapidity at the diffractive cluster kinematical centre, in $p\bar{p}$ SD interactions at $\sqrt{s}$=540 GeV, as a function of the cluster mass. The data[37] from UA4 are compared with the Monte Carlo (continuous curve). The result obtained with a model with isotropic decay of the diffractive cluster (dashed curve) is shown for comparison.

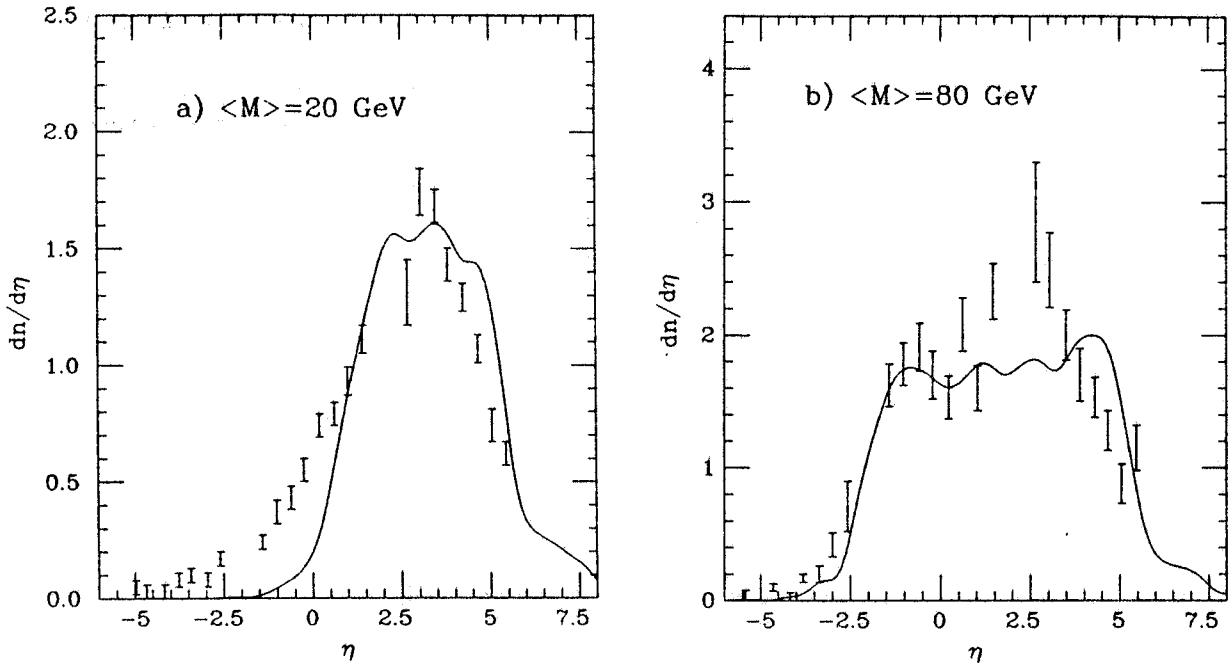

FIG. 11 - Pseudorapidity distribution of charged particles from the decay of diffractive states with mass M (**a**) from 7 to 50 GeV (<M>≈20 GeV) and (**b**) from 72 to 90 GeV (<M>≈80 GeV), in $p\bar{p}$ SD interactions at $\sqrt{s}$=540 GeV. The data[37] from UA4 are compared with the Monte Carlo (continuous curves).

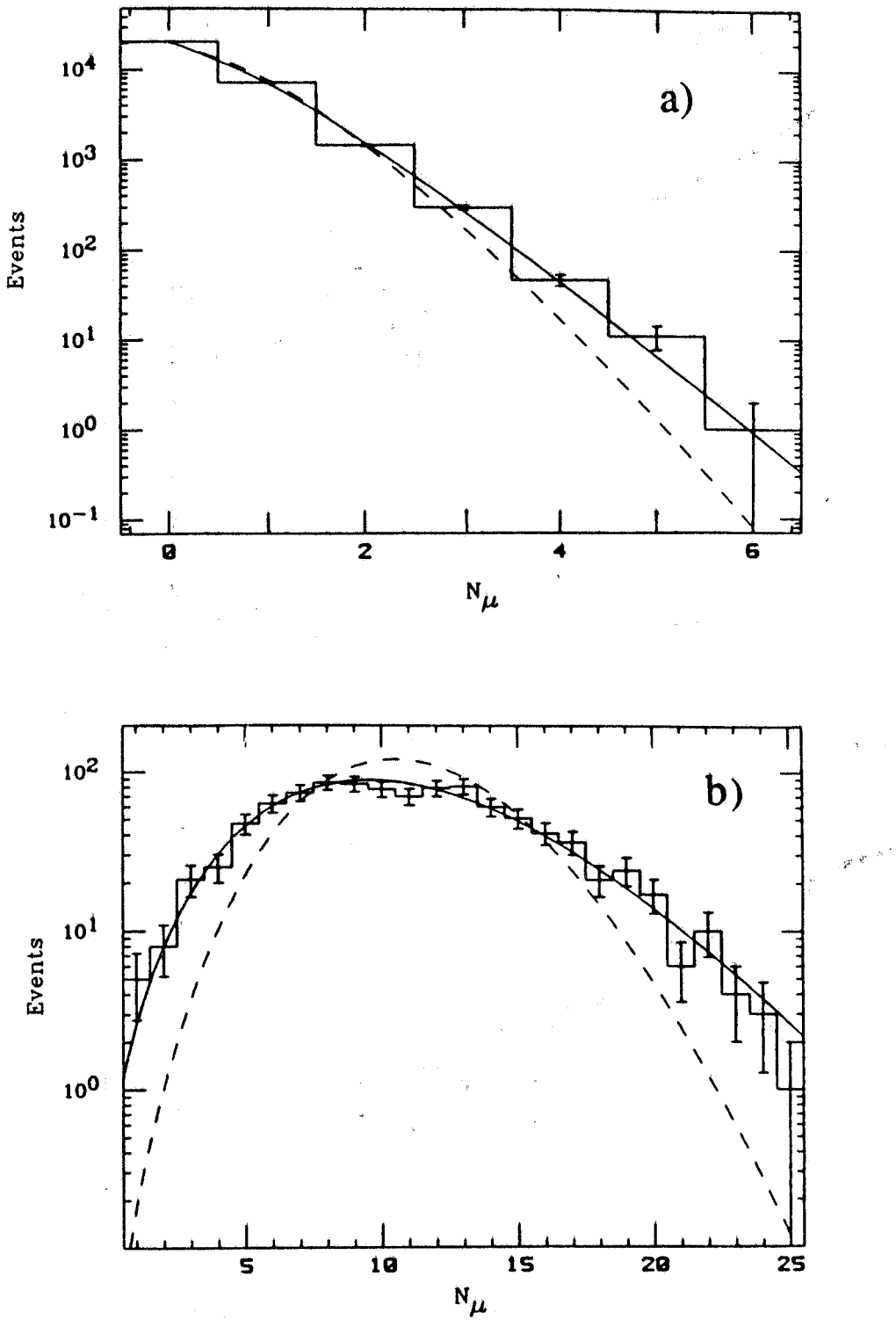

FIG. 12 - Muon multiplicity distribution from primary vertical protons of energy E for rock thickness 3000 hg/cm^2. The histogram (with statistical errors) represents the Monte Carlo result; the continuous curve is the best fit with a negative binomial; the dashed curve is a Poisson distribution with the same average as from the Monte Carlo. a) 30000 showers with E=100 TeV; b) 1000 showers with E=10^4 TeV.

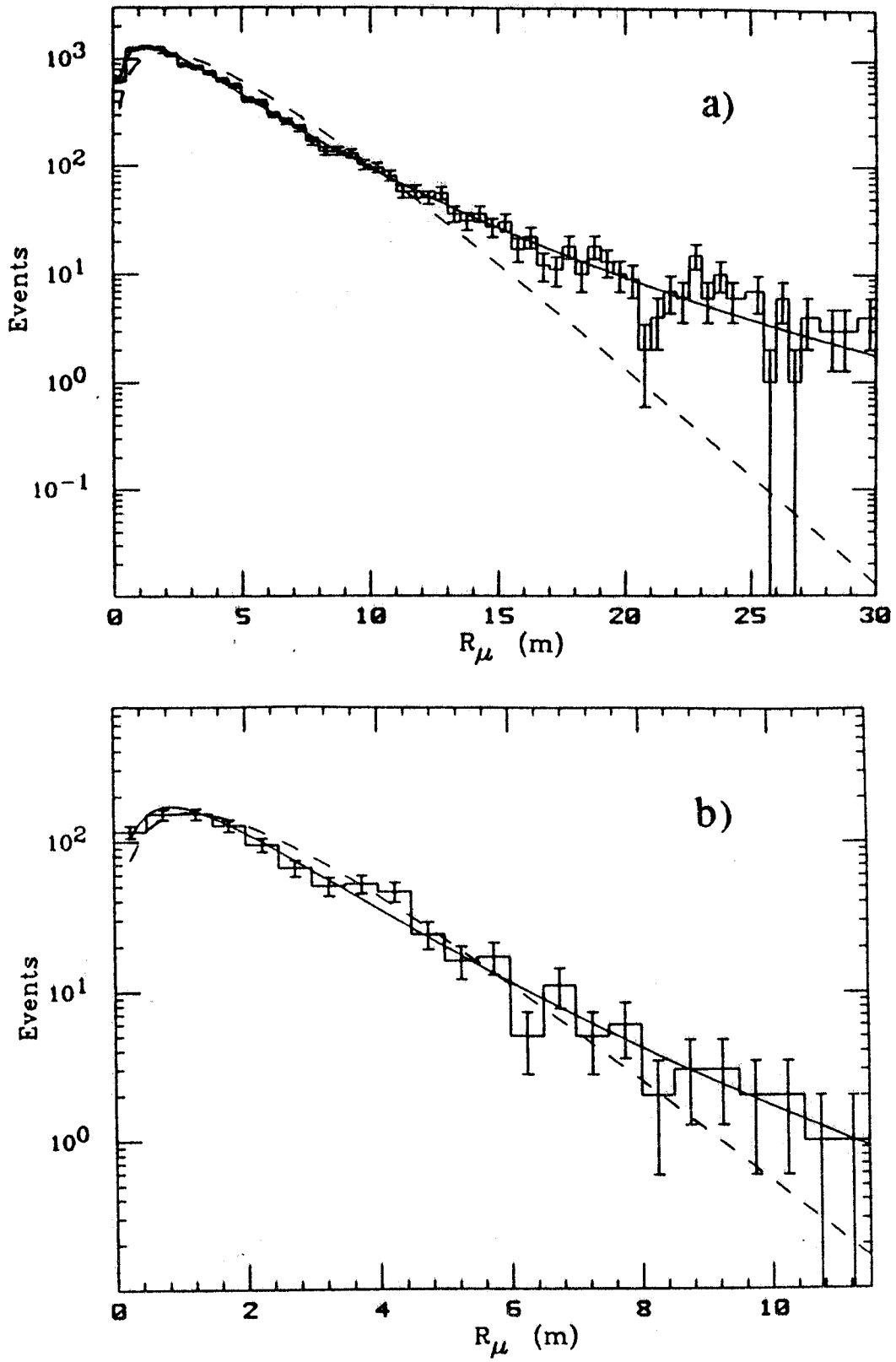

FIG. 13 - Muon lateral distribution (events per ΔR) for 1000 proton showers of energy $E=10^4$ TeV, zenith angle $\theta=28^\circ$ and for rock thickness h. The histogram (with statistical errors) represents the Monte Carlo result; the continuous curve is the best fit with an inverse power-law; the dashed curve is an exponential distribution with the same average as from the Monte Carlo. a) h=3000 hg/cm^2; b) h=6000 hg/cm^2.

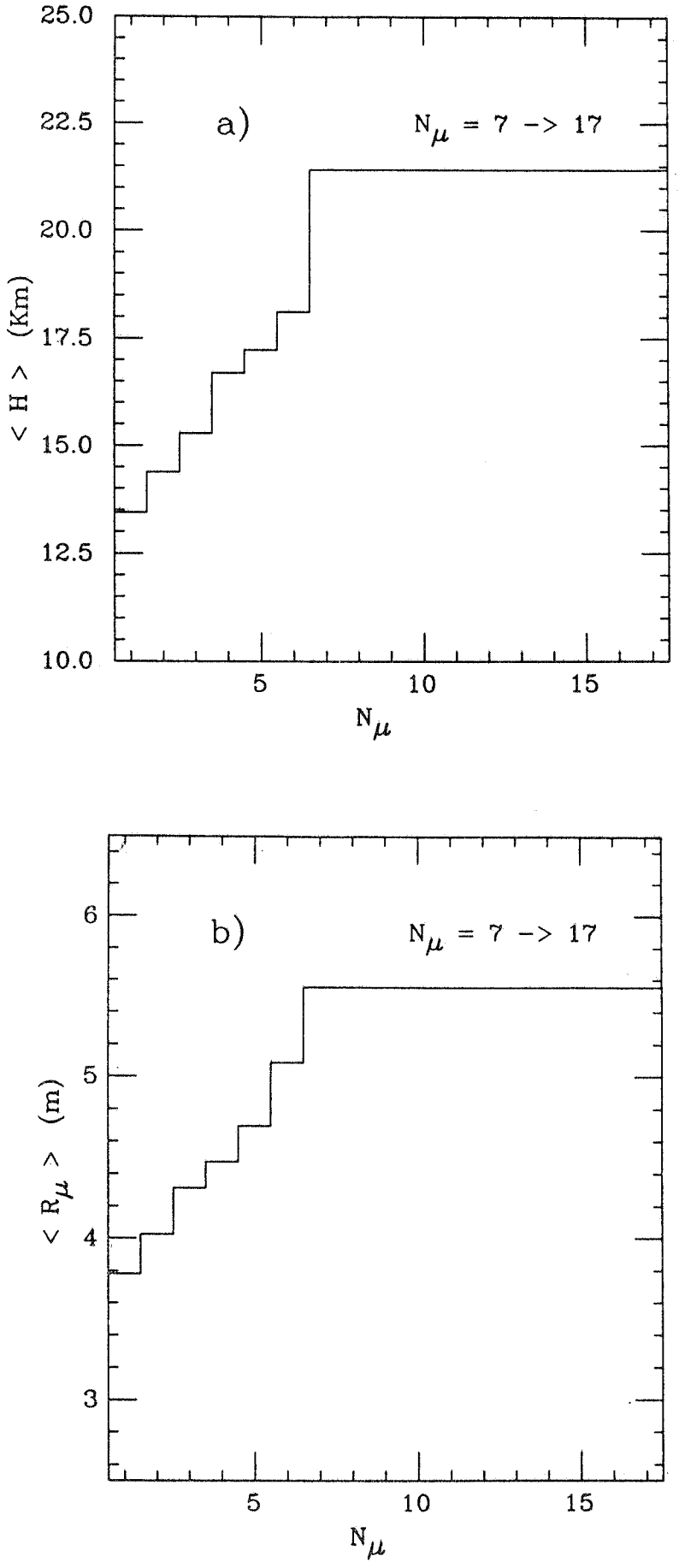

FIG. 14 - Relation among muon multiplicity, height of production and lateral distribution. **a)** Mean slant height of muon origin as a function of muon multiplicity; **b)** Mean perpendicular core distance as a function of muon multiplicity. The results are for proton showers of 1000 TeV at zenith angle 28° observed at a slant depth of 3000 hg/cm^2. The mean core distance for all N_μ is $\langle R_\mu \rangle$=4.60 m. The mean multiplicity is $\langle N_\mu \rangle$=2.26.

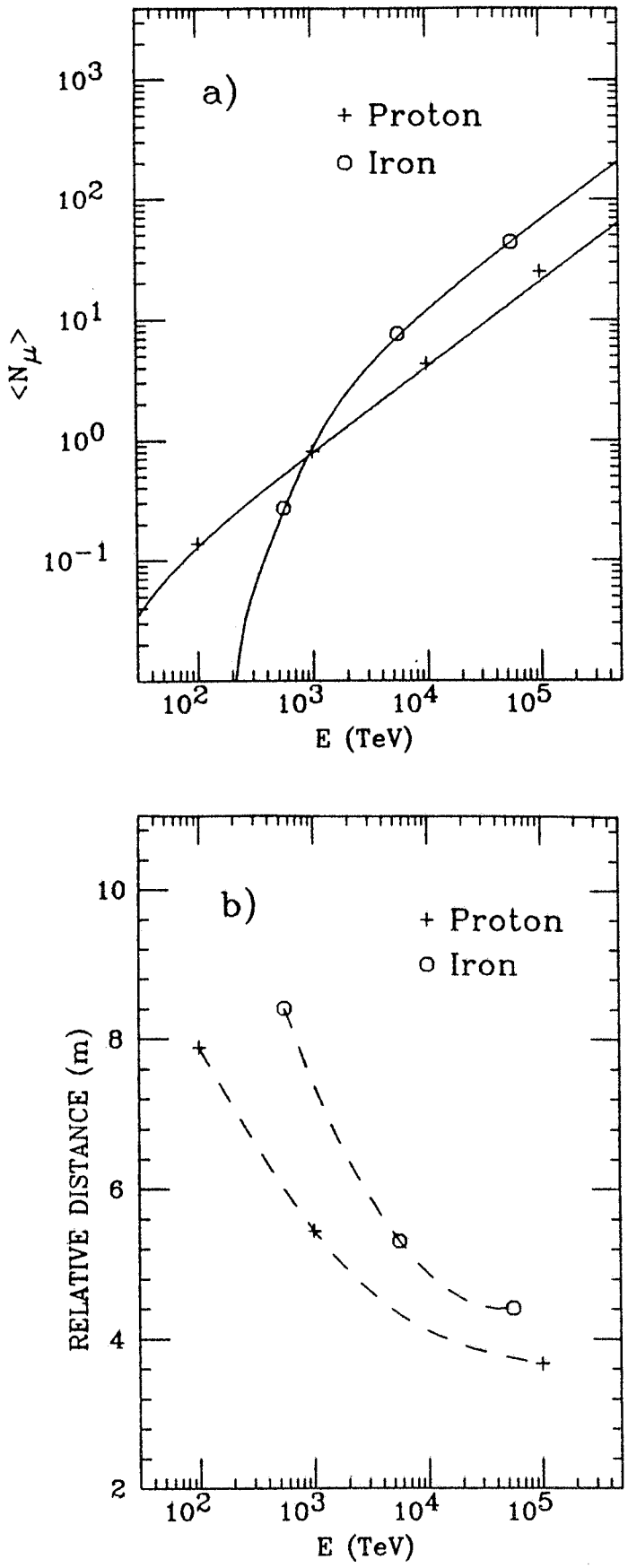

FIG. 15 - Muon multiplicity and separation from Monte Carlo, for vertical showers observed at 4000 hg/cm^2 underground as a function of primary energy for protons and iron nuclei. **a)** Mean multiplicity at the depth of a detector (continuous curves are fits of the Monte Carlo results - Eqs.19-22). **b)** Mean separation between pairs of muons (events with N_μ = n contribute n·(n-1)/2 to this average); dashed curves are drawn only to guide the eye.

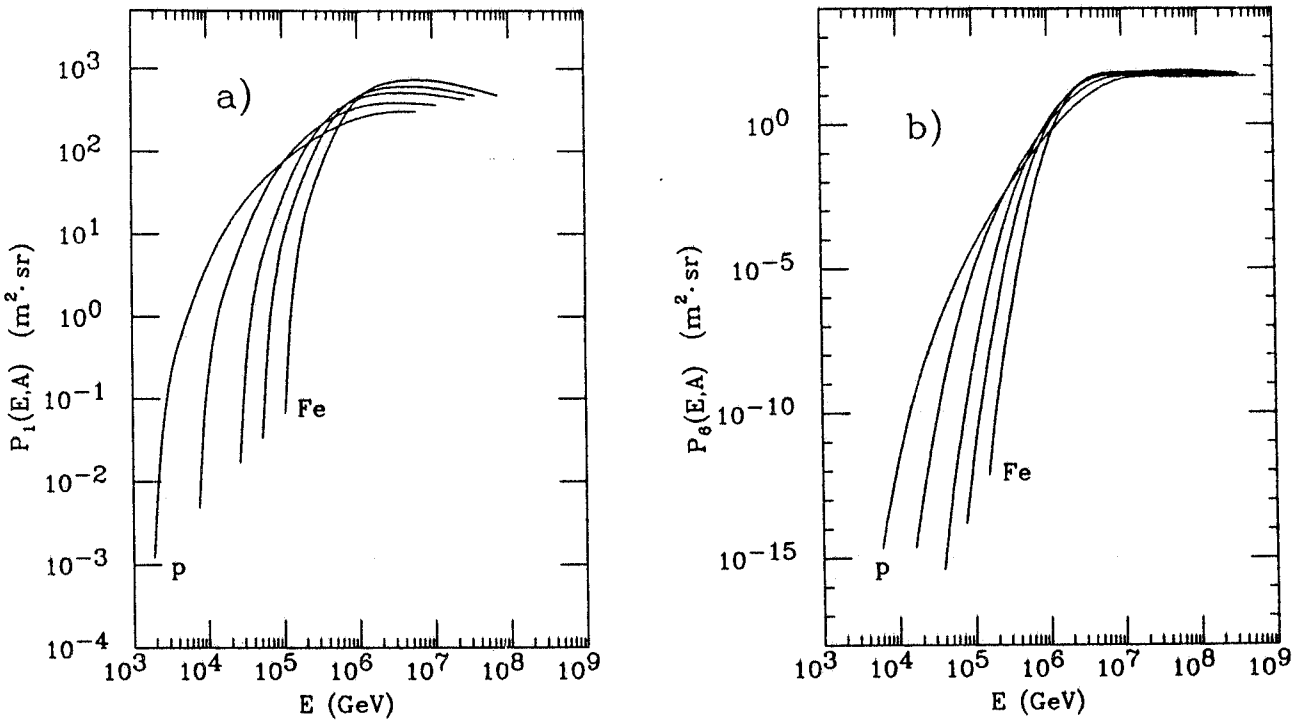

FIG. 16 - $P_N(A, E)$ functions for one SM of the MACRO detector (see text) for the five mass groups; N=1 **(a)**, N=6 **(b)** and N=16 **(c)**. The curves correspond to, from left to right: p, α, CNO, Mg-Si and Fe. Note the change of vertical scale.

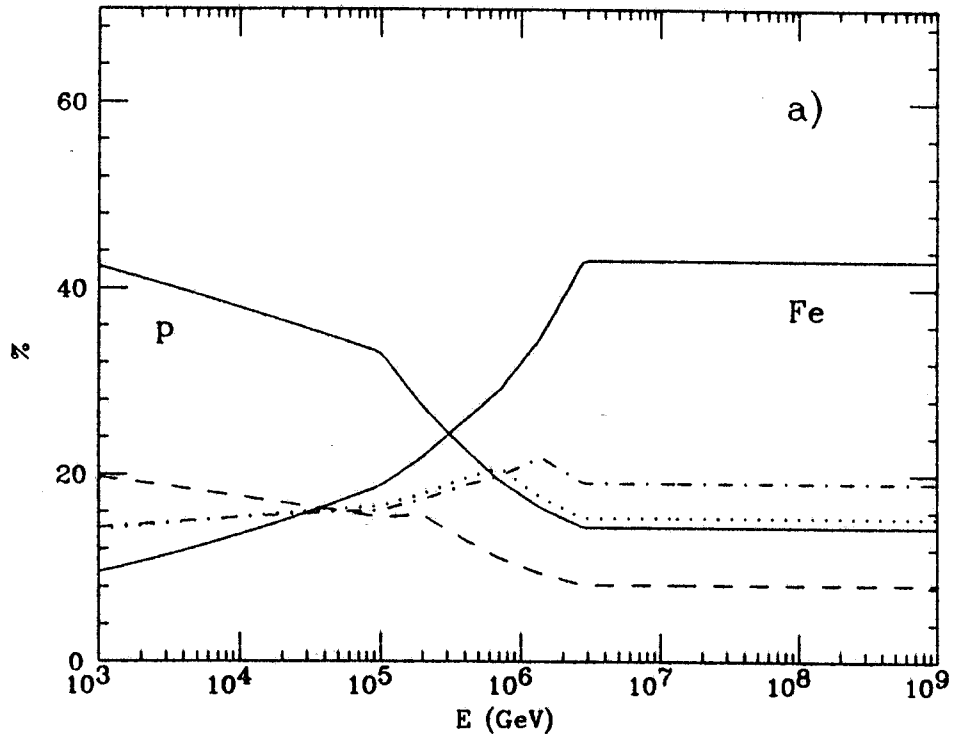

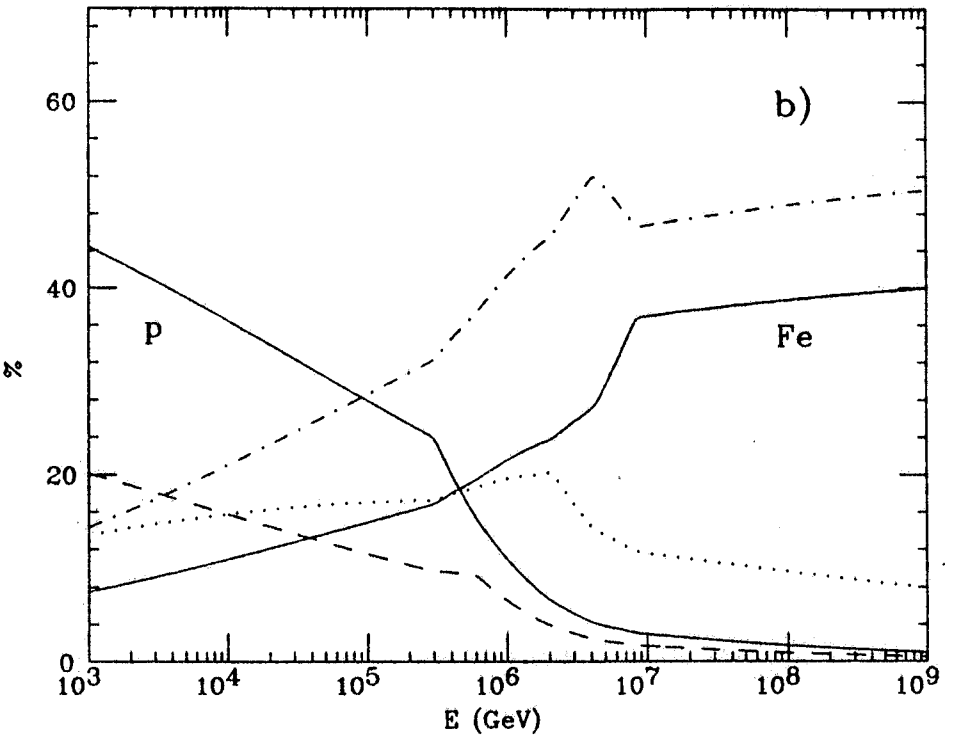

FIG. 17 - The percentage of each mass component as a function of the energy per nucleus, according to the four composition models considered in the text : (a) p-poor, (b) Maryland. The mass components are : p and Fe (continuous curves), α (dashed), CNO (dotted) and Mg-Si (dot-dashed).

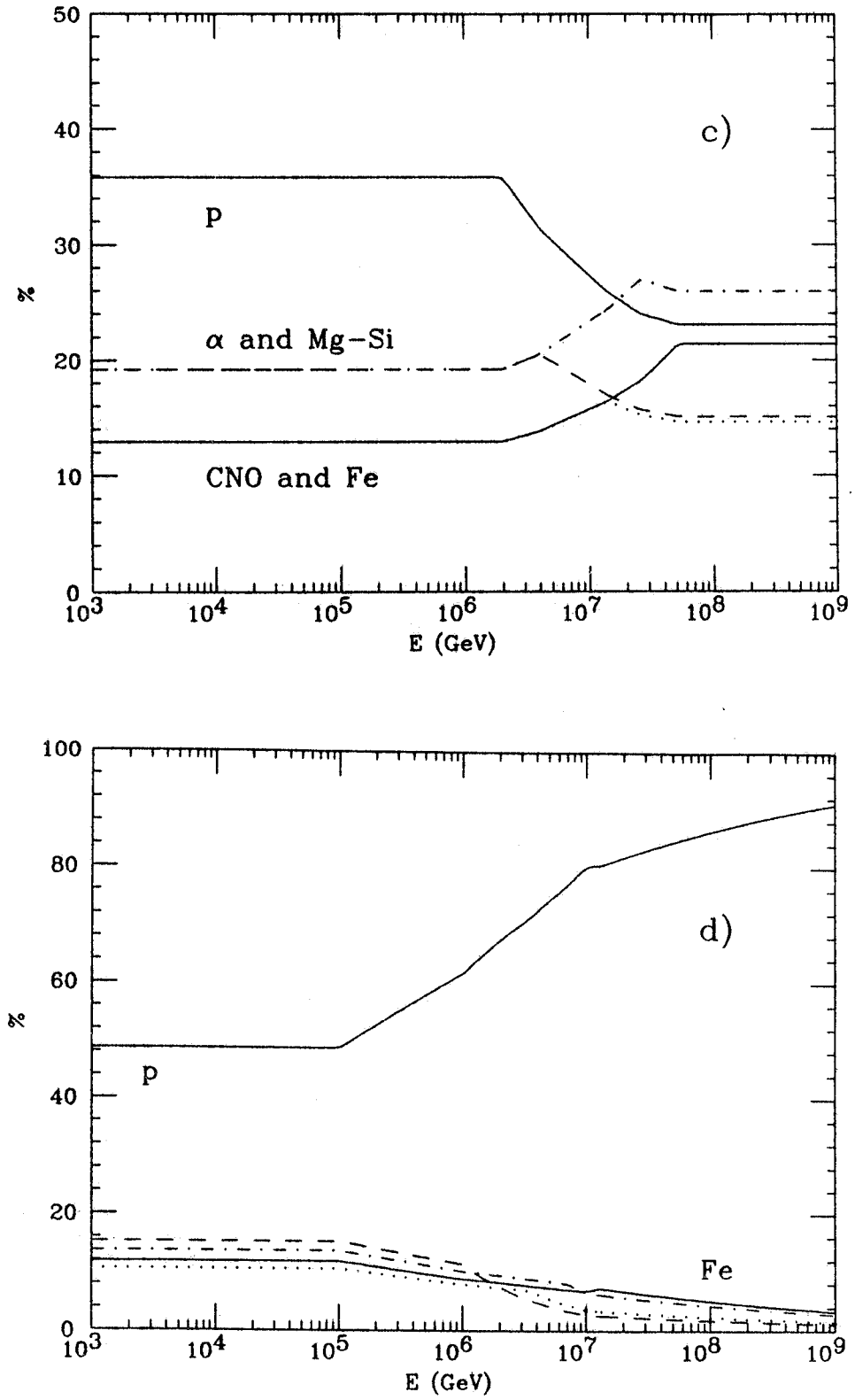

FIG. 17 - The percentage of each mass component as a function of the energy per nucleus, according to the four composition models considered in the text: (c) CMC and (d) Linsley. The mass components are : p and Fe (continuous curves), α (dashed), CNO (dotted) and Mg-Si (dot-dashed).

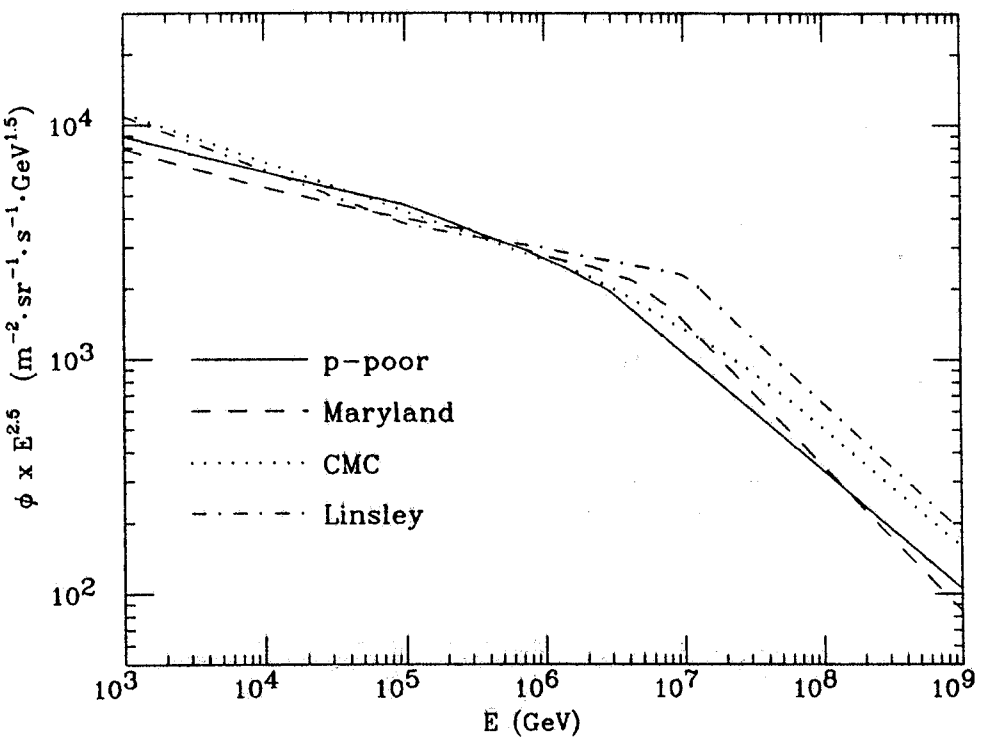

FIG. 18 - All-particle spectra $\phi(E)$ (multiplied by $E^{2.5}$) for the four composition models considered in the text.

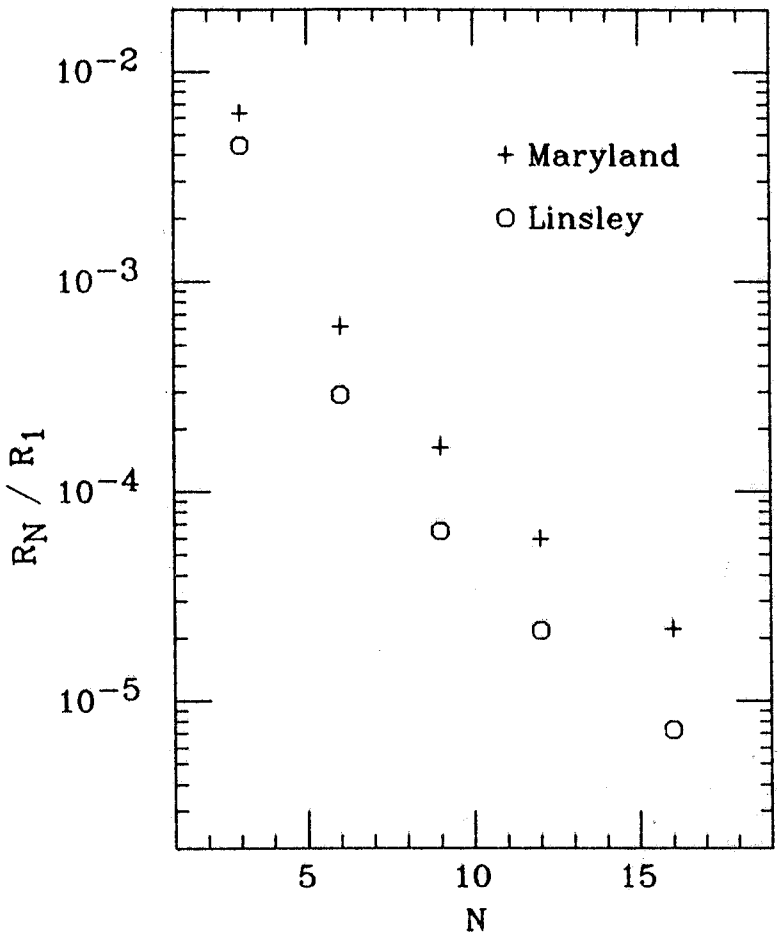

FIG. 19 - Ratio of multiples to singles in one SM, for the Maryland (+) and Linsley (o) composition models.

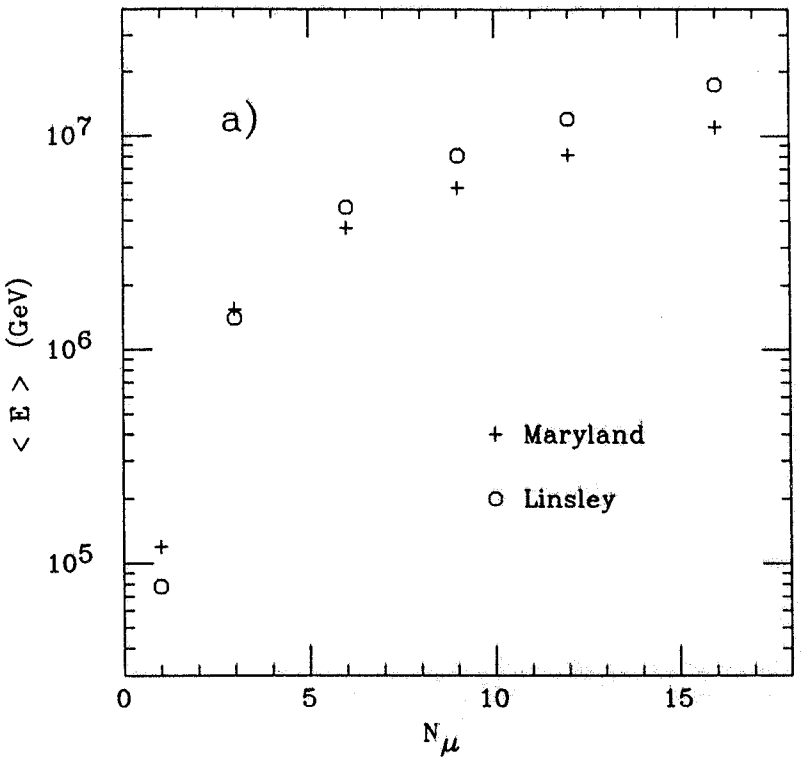

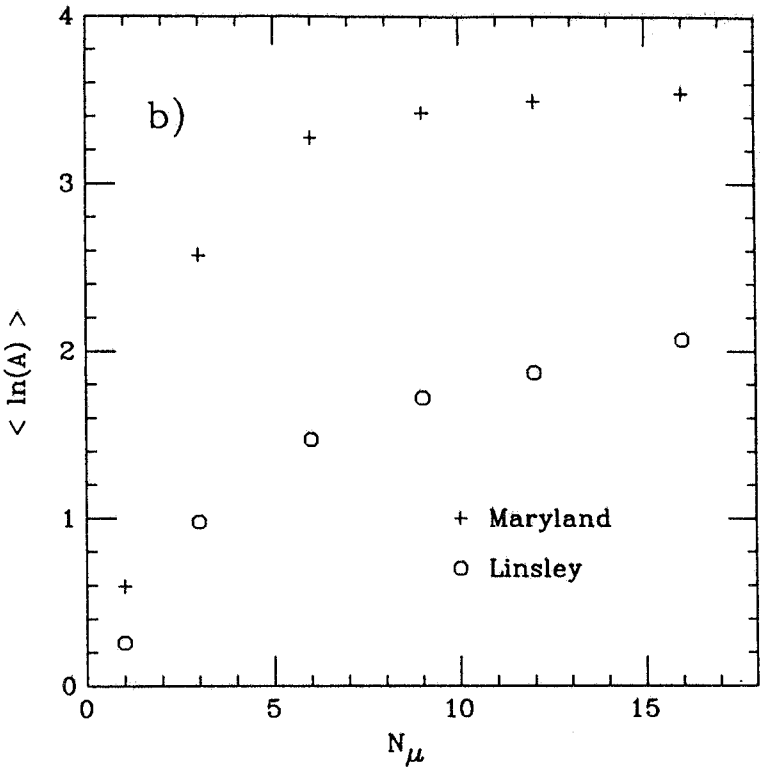

FIG. 20 - (a) Mean primary energy and **(b)** mean primary mass, as functions of the muon multiplicity in one SM, according to the Maryland (+) and Linsley (o) composition models.

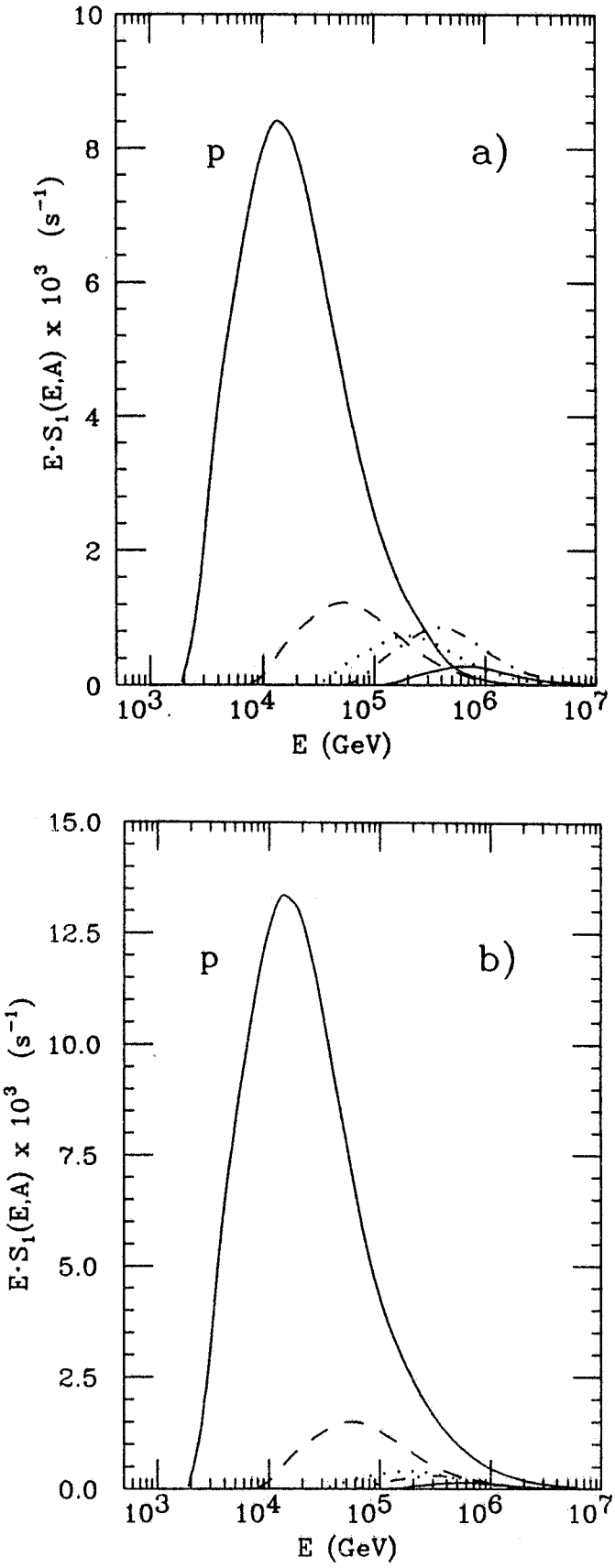

FIG. 21 - Functions $E \cdot S_1(A, E)$ according to the Maryland (**a**) and Linsley (**b**) composition models. The mass components are : p (continuous curve labelled p), α (dashed), CNO (dotted), Mg-Si (dot-dashed) and Fe (non-labelled continuous curve).

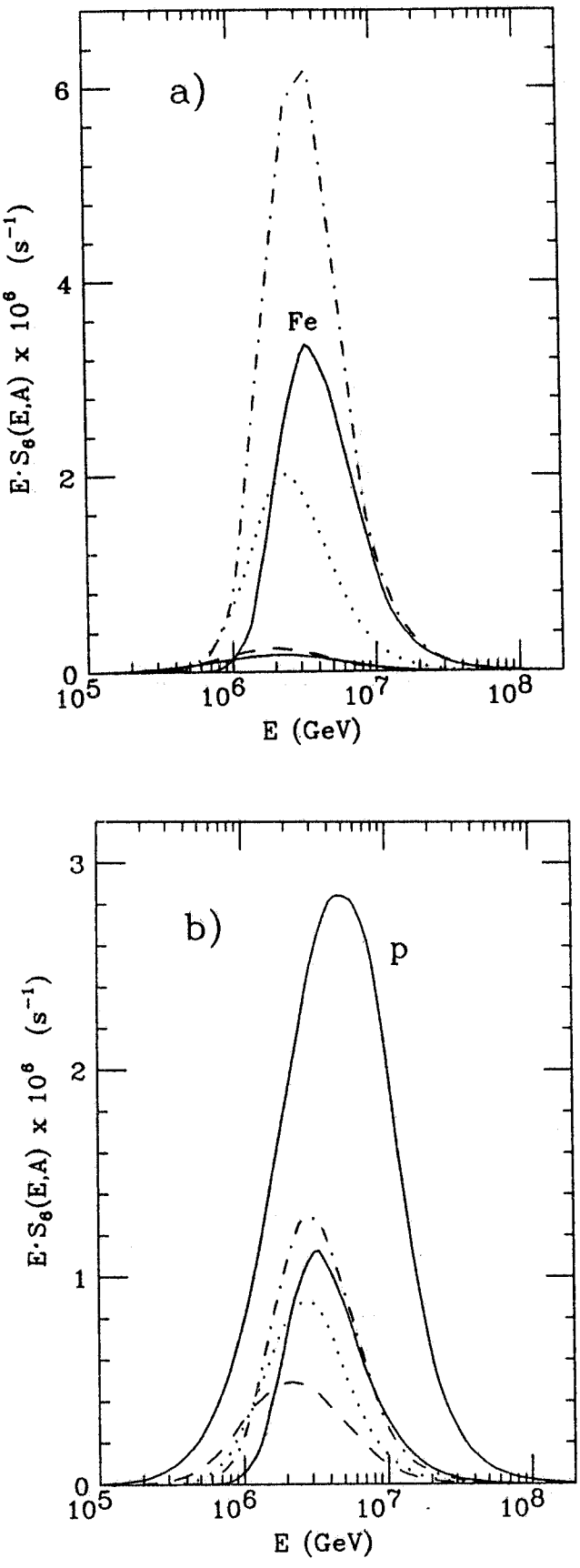

FIG. 22 - Functions $E \cdot S_6(A, E)$ according to the Maryland (a) and Linsley (b) composition models. The mass components are : p and Fe (continuous curves), α (dashed), CNO (dotted) and Mg-Si (dot-dashed).

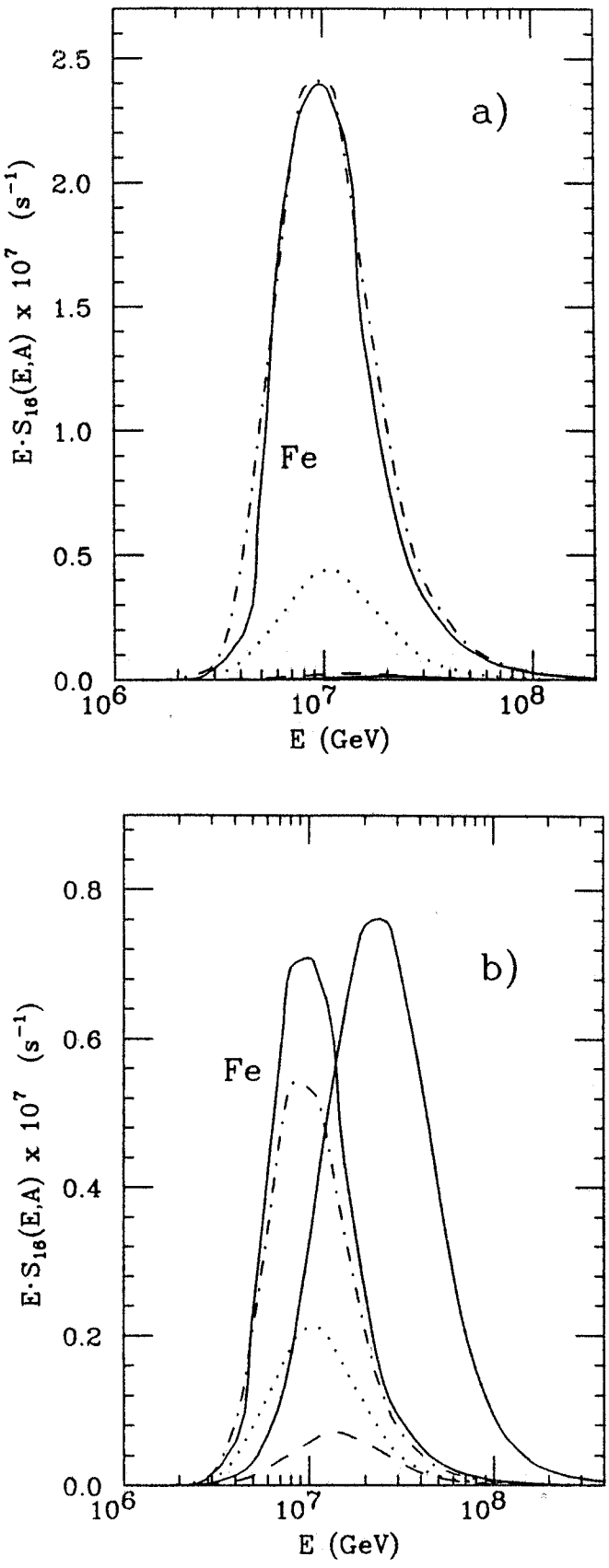

FIG. 23 - Functions $E \cdot S_{16}(A, E)$ according to the Maryland (**a**) and Linsley (**b**) composition models. The mass components are : p (non-labelled continuous curves), α (dashed), CNO (dotted), Mg-Si (dot-dashed) and Fe (continuous curves labelled Fe).

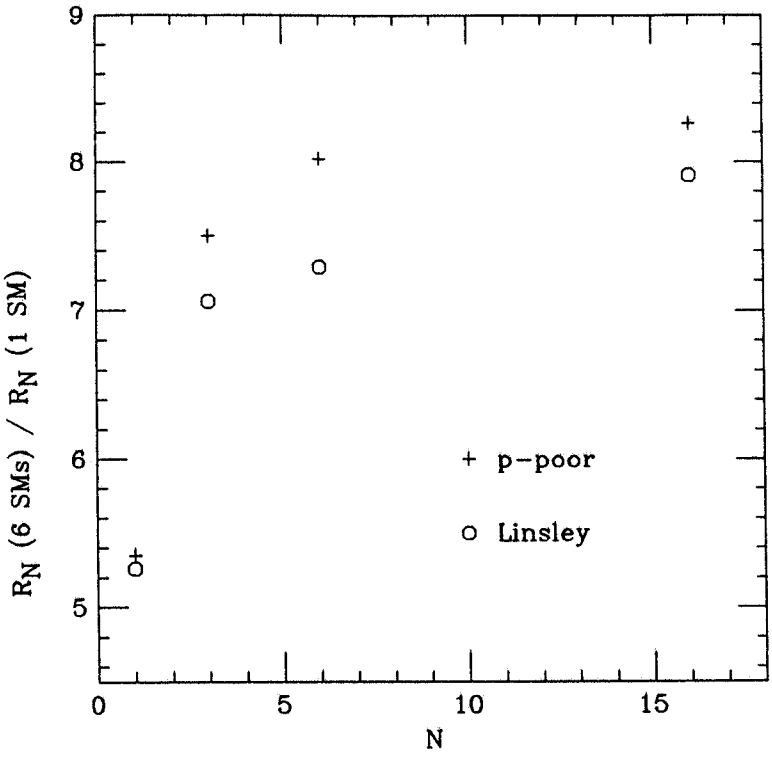

FIG. 24 - Ratio between the rates R_N(6 SMs) obtained with six SM's and the rates R_N(1 SM) obtained with one SM, as a function of the muon multiplicity N, according to the p-poor (+) and Linsley (o) composition models.

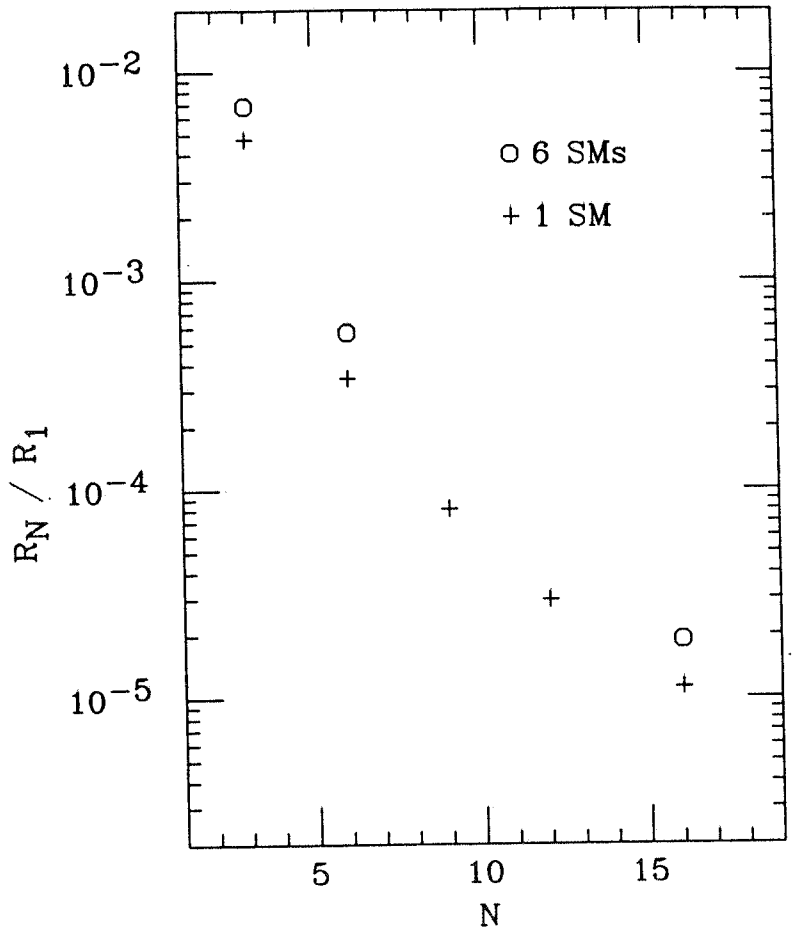

FIG. 25 - Ratio of multiples to singles in one SM (+) and in six SM's (o), for the CMC composition model.

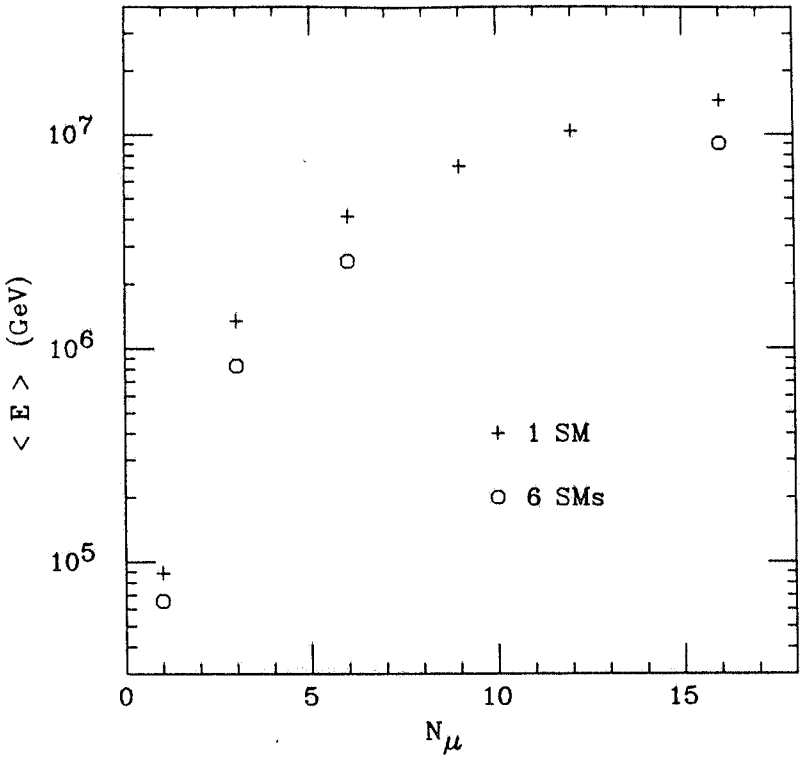

FIG. 26 - Mean primary energy as a function of the muon multiplicity in one SM (+) and in six SM's (o), according to the CMC composition model.

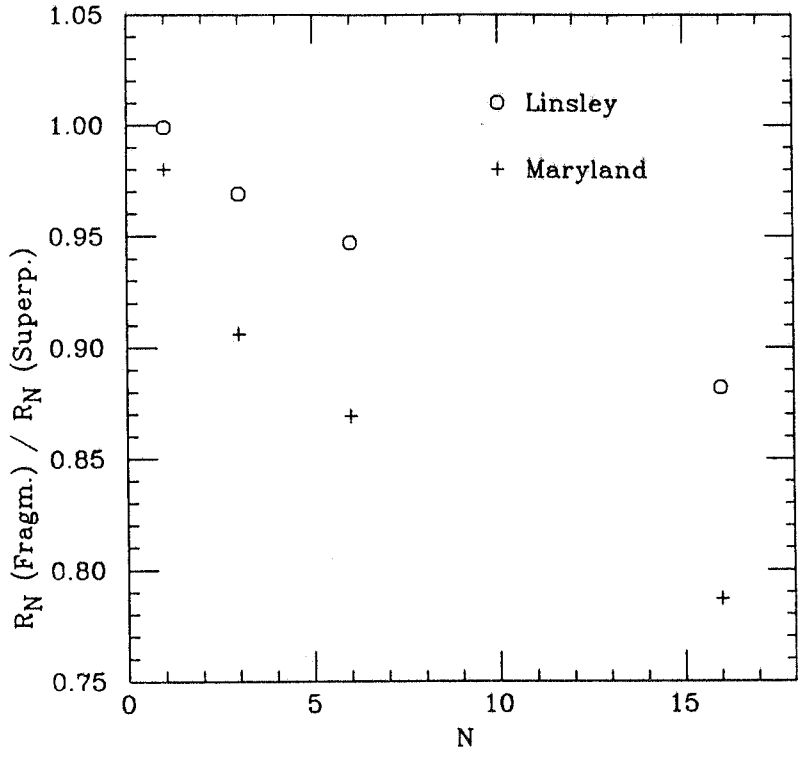

FIG. 27 - Ratio of the rates in one SM with fragmentation effects (see text) to the rates with the "superposition model".